# Proximal immune-epithelial progenitor interactions drive chronic tissue sequelae post COVID-19

Harish Narasimhan[1-3]*, In Su Cheon[1,2]*, Wei Qian[1,2]*, Sheng'en Hu*[4], Tanyalak Parimon*[5,6], Chaofan Li[1,2], Nick Goplen[7], Yue Wu[1,2], Xiaoqin Wei[1,2], Young Min Son[8], Elizabeth Fink[1,2], Gislane Santos[1,2], Jinyi Tang[1,2], Changfu Yao[5,6], Lyndsey Muehling[9], Glenda Canderan[9], Alexandra Kadl[10], Abigail Cannon[1,2], Patcharin Pramoonjago[11], Yun Michael Shim[10], Judith Woodfolk[9], Chongzhi Zang[4#], Peter Chen[5,6#] and Jie Sun[1-3#]

1. Beirne B. Carter Center for Immunology Research, University of Virginia, Charlottesville, VA 22908, USA.
2. Division of Infectious Disease and International Health, Department of Medicine, University of Virginia, Charlottesville, VA 22908, USA.
3. Department of Microbiology, Immunology and Cancer Biology, University of Virginia, Charlottesville, VA 22908, USA.
4. Center for Public Health Genomics, University of Virginia School of Medicine, Charlottesville, VA 22908, USA.
5. Women's Guild Lung Institute, Department of Medicine, Cedars-Sinai Medical Center, Los Angeles, CA 90048, USA.
6. Department of Biomedical Sciences, Cedars-Sinai Medical Center, Los Angeles CA 90048, USA.
7. Robert and Arlene Kogod Center on Aging, Mayo Clinic, Rochester, MN 55905, USA.
8. Department of Systems Biotechnology, Chung-Ang University, Anseong, Korea.
9. Division of Asthma, Allergy and Immunology, Department of Medicine, University of Virginia, Charlottesville, VA 22908, USA.
10. Division of Pulmonary and Critical Care Medicine, Department of medicine, University of Virginia, Charlottesville, VA 22908, USA.
11. School of Medicine, University of Virginia, Charlottesville, VA 22908, USA.

*** Co-first authors**

**# Co-correspondent authors:**

**J.S.:** js6re@virginia.edu

**P.C.:** Peter.Chen@cshs.org

**C.Z.:** zang@virginia.edu

**ABSTRACT**

The long-term health effects of SARS-CoV-2, termed Post-Acute Sequelae of COVID-19 (PASC), are quickly evolving into a major public health concern, but the underlying cellular and molecular etiology remain poorly defined. There is growing evidence that PASC is linked to abnormal immune responses and/or poor organ recovery post-infection. However, the exact processes linking non-resolving inflammation, impaired tissue repair, and PASC are still unclear. In this report, we utilized a cohort of respiratory PASC patients with viral infection-mediated pulmonary fibrosis and a clinically relevant mouse model of post-viral lung sequelae to investigate the pathophysiology of respiratory PASC. Using a combination of imaging and spatial transcriptomics, we identified dysregulated proximal interactions between immune cells and epithelial progenitors unique to respiratory PASC but not acute COVID-19 or idiopathic pulmonary fibrosis (IPF). Specifically, we found a central role for lung-resident $CD8^+$ T cell-macrophage interactions in maintaining $Krt8^{hi}$ transitional and ectopic $Krt5^+$ basal cell progenitors, and the development of fibrotic sequelae after acute viral pneumonia. Mechanistically, $CD8^+$ T cell derived IFN-γ and TNF stimulated lung macrophages to chronically release IL-1β, resulting in the abnormal accumulation of dysplastic epithelial progenitors in fibrotic areas. Notably, therapeutic neutralization of IFN-γ and TNF, or IL-1β after the resolution of acute infection resulted in markedly improved alveolar regeneration and restoration of pulmonary function. Together, our findings implicate a dysregulated immune-epithelial progenitor niche in driving respiratory PASC and identify potential therapeutic targets to dampen chronic pulmonary sequelae post respiratory viral infections including SARS-CoV-2.

## INTRODUCTION

SARS-CoV-2 infection can lead to long-term pulmonary and extrapulmonary symptoms well beyond the resolution of acute disease, a condition collectively termed post-acute sequelae of SARS-CoV-2 (PASC) (1, 2). With effective treatment strategies and vaccines to tackle acute COVID-19, the emerging challenge is to manage chronic sequelae in the 60+ million people currently experiencing PASC (3, 4). Given the extensive damage to the respiratory tract during primary infection, the lungs are particularly susceptible to sustained impairments including dyspnea, compromised lung function, and radiological abnormalities which persist up to 2 years post infection in contrast to the majority of extrapulmonary sequelae (1, 2, 4). Some individuals also develop a non-resolving fibroproliferative response – PASC pulmonary fibrosis (PASC-PF) and typically require persistent oxygen supplementation and eventual lung transplantation (4-8). Despite progress in identifying dysregulated immune signatures associated with respiratory PASC (3, 7, 9-16), little is known regarding their mechanistic roles in driving pathological tissue sequelae, in part due to the lack of studies adopting “clinically relevant” animal models of respiratory PASC.

It has long been established that, type 2 alveolar epithelial (AT2) cells are the facultative stem cell of the lungs that undergo self-renewal and differentiate into type 1 alveolar (AT1) cells to replenish the denuded epithelial niche after alveolar injury (17-19). Recent work has further delineated the AT2 to AT1 trans-differentiation process and identified a transitional state characterized by high expression of cytokeratin 8 ($Krt8^{hi}$) (18-22). Severe alveolar damage also induces the recruitment of $Krt5^{+}$ basal cell progenitors to the distal lung, which persist in an undifferentiated state or differentiate into upper airway cell fates, causing alveolar “bronchiolization” (23-27). The accumulation of undifferentiated $Krt8^{hi}$ transitional cells and/or the emergence of ectopic $Krt5^{+}$ pods are hallmarks of lung injury, and their persistence have pathologically been associated with chronic diseases such as lung fibrosis (5, 28-33).

Currently, mechanisms underlying the maintenance of these dysplastic progenitors and their contributions to post-viral respiratory sequelae remain largely elusive. By comparing the pathological, immunological, and molecular features of human respiratory PASC and mouse models of post-viral lung sequelae, here we have discovered that spatially defined interactions among $CD8^{+}$ T cells, macrophages, and epithelial progenitors drive chronic tissue sequelae

after acute viral injury. Furthermore, we identify nodes for therapeutic intervention, which may be adopted in the clinic to mitigate chronic pulmonary sequelae after COVID-19.

## METHODS

### Ethics and biosafety

All aspects of this study were approved by the Institutional Review Board Committee at Cedars-Sinai Medical Center (IRB# Pro00035409) and the University of Virginia (IRB# 13166). Work related to SARS-CoV-2 was performed in animal biosafety level 3 (ABSL-3) facilities at the University of Virginia and influenza-related experiments were performed in animal biosafety level 2 (ABSL-2) facilities at the Mayo Clinic and the University of Virginia.

### Cells, viruses, and mice

African green monkey kidney cell line Vero E6 (ATCC CRL-1587) were maintained in Dulbecco modified Eagle medium (DMEM) supplemented with 10% fetal bovine serum (FBS), along with 1% of penicillin-streptomycin (P/S) and L-glutamine at 37°C in 5% $CO_2$. The SARS-CoV-2 mouse-adapted strain (MA-10) was kindly provided by Dr. Barbara J Mann (University of Virginia School of Medicine). The virus was passaged in Vero E6 cells, and the titer was determined by plaque assay using Vero E6 cells.

Young (8–10-week-old) and aged (84-week-old) female C57BL/6J mice, and 15-week-old female BALB/cJ mice were purchased from The Jackson Laboratory (JAX). WT C57BL/6 (catalog no. 000664) mice were purchased from the Jackson Laboratory and bred in-house. Aged mice were received at 20 to 21 months of age from the National Institutes of Aging and all mice were maintained in the facility for at least 1 month before infection. All mice were housed in a specific pathogen–free environment and used under conditions fully reviewed and approved by the institutional animal care and use committee guidelines at the Mayo Clinic (Rochester, MN) and University of Virginia (Charlottesville, VA).

For primary influenza virus infection, influenza A/PR8/34 strain [75 plaque-forming units (PFU) per mouse] was diluted in fetal bovine serum (FBS)–free Dulbecco's modified Eagle's medium (DMEM) (Corning) on ice and inoculated in anesthetized mice through intranasal route as described previously (34). For SARS-CoV-2 infections, mice were infected with 5 x $10^4$ PFU for C57/BL6 and 1000PFU for BALB/c virus of mouse-adapted (MA-10) intranasally under anesthesia as described previously. Infected mice were monitored daily for weight loss and clinical signs of disease for 2 weeks, following once a week for the duration of the experiments.

The mortality rate of mice calculated as “dead” were either found dead in cage or were euthanized as mice reached 70% of their starting body weight which is the defined humane endpoint in accordance with the respective institutional animal protocols. At the designated endpoint, mice were humanely euthanized by ketamine/xylazine overdose and subsequent cervical dislocation.

### *In vivo* drug treatment

For depletion of $CD8^+$ T cells and neutralization of cytokines, starting at 21 dpi, mice were intraperitoneally administered 500 µg of anti-CD8 Ab (53-6.7 and 2.43; BioXCell), anti-IL-1β (B122; BioXCell), anti-IFNγ (XMG1.2; BioXCell), anti-TNFα (XT3.11; BioXCell) or isotype control immunoglobulin G (IgG) in 200µL of phosphate-buffered saline (PBS) once a week. Mice were euthanized 3 days after the last treatment.

### Evaluation of respiratory mechanics and lung function

Lung function measurements using FOT and the resulting parameters have been previously described (35). In brief, animals were anesthetized with an overdose of ketamine/xylazine (100 and 10mg/kg intraperitoneally) and tracheostomized with a blunt 18-gauge canula (typical resistance of 0.18 $cmH_2O$ s/mL), which was secured in place with a nylon suture. Animals were connected to the computer-controlled piston (SCIREQ flexiVent), and forced oscillation mechanics were performed under tidal breathing conditions described in (35) with a positive-end expiratory pressure of 3 cm $H_2O$. The measurements were repeated following thorough recruitment of closed airways (two maneuvers rapidly delivering TLC of air and sustaining the required pressure for several seconds, mimicking holding of a deep breath). Each animal’s basal conditions were normalized to their own maximal capacity. Measurement of these parameters before and after lung inflation allows for determination of large and small airway dysfunction under tidal (baseline) breathing conditions. Only measurements that satisfied the constant-phase model fits were used (>90% threshold determined by software). After this procedure, mice had a heart rate of ~60 beats per minute, indicating that measurements were done on live individuals.

### Human lung tissue specimens

Human lung samples were obtained from patients enrolled in the IRB-approved Lung Institute BioBank (LIBB) study at Cedars-Sinai Medical Center, Los Angeles, CA. All participants or their legal representatives provided informed written consent. Lung tissues were processed within 24

hours after surgical removal. Specifically, the lung tissues were cut and immediately fixed in 10% normal-buffered formalin for 24 hours before tissue processing using the HistoCore PEARL – Tissue Processor, Leica Biosystem, Deer Park, IL, and embedded in paraffin for histological studies. The formalin-fixed paraffin-embedded cassettes were properly stored at room temperature until further sectioning.

**Mouse tissue processing and flow cytometric analysis:**

Animals were injected intravenously with 4 µg of CD45 or 2 µg of CD90.2 Ab labeled with various fluorochromes. Two minutes after injection, animals were euthanized with an overdose of ketamine/xylazine and processed 3 min later. After euthanasia, the right ventricle of the heart was gently perfused with chilled 1X PBS (10 mL). Right lobes of the lungs were collected in 5 mL of digestion buffer (90% DMEM and 10% PBS and calcium with type 2 collagenase (180 U/ml) (Worthington) and DNase (15 µg/ml) (Sigma-Aldrich) additives). Tissues were digested at 37°C for 1 hour followed by disruption using gentleMACS tissue dissociator (Miltenyi). Single-cell suspension were obtained by hypotonic lysis of red blood cells in ammonium-chloride-potassium buffer and filtration through a 70µm mesh. Cells were washed with FACS buffer (2% of FBS and 0.1% of $NaN_3$ in PBS) and FC-γ receptors were blocked with anti-CD16/32 (2.4G2). Surface staining was performed by antibody (details provided in **Supplementary Table 2**) incubation for 30 min at 4°C in the dark. After PBS wash, cells were resuspended with Zombie-dye (Biolegend) and incubated at RT for 15 min. For IL-1β staining, cells were incubated with monesine (Biolegend) for 5 hours at 37°C and then stained with surface markers antibodies. After washing with FACS buffer, cells were fixed with fixation buffer (Biolegend) and permeabilized with intracellular staining permeabilization wash buffer (Biolegend). The cells were then stained with anti-IL-1β at RT for 1hr and samples were acquired on an Attune NxT (Life Technologies). The data were analyzed with FlowJo software (Tree Star).

**Caspase 1 FLICA analysis**

Caspase 1 was detected by FAM-FLICA Caspase-1 Assay Kit (ImmunoChemistry Technologies) according to the manufacturer's instructions. Briefly, lung single cells or macrophages from *in vitro* culture were stained with fluorochrome-conjugated Ab cocktail for cell surface markers. After staining, cells were incubated with FLICA for 30min at 37°C, washed and detected by flow cytometry.

**Cell isolation and *ex vivo* co-culture**

To isolate myeloid and $CD8^+$ T cells, single cell suspension of the lung was generated from influenza infected mice as described above and labeled and enriched with CD11c and CD11b or CD8 microbeads (Miltenyi Biotec, Auburn, CA) according to the manufacturer's instructions. Purified myeloid cells were seeded in 96-well (200,000 per well) plates and incubated for 2 hours at 37°C 5% $CO_2$ to facilitate attachment. Wells were washed with 1X PBS to select for macrophages, following which selected wells were seeded with naïve or memory $CD8^+$ T cells (40,000 per well) and further incubated for 16-18 hours. Supernatant and cell pellets were collected for cytokine measurement and gene expression analyses, respectively.

**AT2 cell isolation and culture**

AT2 cells were isolated from naïve mice as previously described (26, 36, 37). Briefly, mouse lungs were perfused with chilled PBS and intratracheally instilled with 1mL of dispase II (15U/mL, Roche), tying off the trachea and cutting away the lobes from the mainstem bronchi. Lungs were incubated in 4mL of 15U/mL dispase II for 45min while shaking at room temperature, followed by mechanical dissociation with an 18G needle**.** Following passage through a 100µm filter, lungs underwent 10min of DNase I digestion (50µg/mL) and filtered through 70µm filter prior to RBC lysis. Single-cell suspensions were subject to CD45 depletion using microbeads (Miltenyi), incubated with anti-FcgRIII/II (Fc block) and stained with CD45, EpCAM, MHC-II, and viability die (see antibody details in **Supplementary Table 2**). Fluorescence assisted cell sorting was performed on the BD Influx cell sorter to isolate AT2 cells as described previously (36) and collected in 500µL DMEM + 40% FBS + 2% P/S. Sorted AT2 cells ($2x10^5$/well) were plated in a 96-well plate in DMEM/F12 + 10% FBS and cultured at 37°C, 5% $CO_2$ for 3 days prior to harvest.

**RNA isolation and real time-quantitative polymerase chain reaction (RT-qpCR)**

Cells were lysed in Buffer RLT and RNA was purified using the RNeasy Plus Mini Kit (Qiagen) according to the manufacturer's instructions. Random primers (Invitrogen) and MMLV reverse transcriptase (Invitrogen) were used to synthesize first-strand complementary DNAs (cDNAs) from equivalent amounts of RNA from each sample. cDNA was used for real-time PCR with Fast SYBR Green PCR Master Mix (Applied Biosystems). Real-time PCR was conducted on QuantStudio 3 (Applied Bioscience). Data were generated with the comparative threshold cycle (Δ*C*t) method by normalizing to hypoxanthine-guanine phosphoribosyltransferase (HPRT) transcripts in each sample as reported previously (38).

**COVID-19 convalescents cohort**

Peripheral blood specimens were obtained from patients presenting to the University of Virginia Post-COVID-19 clinic. All participants provided written informed consent. Pulmonary function testing (PFT: spirometry, lung volume testing, diffusing capacity of the lungs for carbon monoxide [DLCO]) at the time of blood draws was used to define normal and abnormal lung function.

**IL-1β cytokine evaluation**

Plasma from COVID-19 convalescents, supernatant from *ex vivo* culture and murine BAL fluid following flushing of airway 3X with 600uL of sterile PBS were used to quantify IL-1β levels by ELISA as per manufacturer's instructions (R&D systems). Samples were first concentrated 5X (BAL) and 2X (cell culture supernatant) using Microcon-10kDa centrifugal filters (Millipore Sigma).

**Immunofluorescence**

Mouse lung tissues were routinely perfused with ice cold 1X PBS, fixed with 10% formalin and embedded in paraffin. Lung tissue sections (5μm) were deparaffinized in xylene and rehydrated. Heat-induced antigen retrieval was performed using 1X Agilent Dako target retrieval solution (pH 9) in a steamer for 20min (mouse lungs) or 45min (human lungs), followed by blocking and surface staining. For intracellular targets, tissues were permeabilized with 0.5% Triton-X 0.05% Tween20 for 1 hour at room temperature. Sections were stained with primary antibodies as listed in **Supplementary Table 2** overnight at 4°C. Subsequently, samples were washed and incubated with fluorescent secondary antibodies as listed in **Supplementary Table 2** for 2 hours at room temperature. Sections were counterstained with DAPI (1:1000, ThermoFisher Scientific) for 3 minutes and mounted using ProLong Diamond Antifade mountant (ThermoFisher Scientific). After 24 hours of curing at room temperature, images were acquired using the Olympus BX63 fluorescent microscope and pseudocolours were assigned for visualization. For each lung section, images were taken in at least 10-12 random areas in the distal lung. All images were further processed using ImageJ Fiji, OlyVIA, and/or QuPath software.

**Spatial Transcriptomics analyses**

Spatial transcriptomics (ST) data (generated from 10X Visium platform) was pre-processed using the spaceranger package (v2.0, genome version mm10). The Rpackage Seurat (v4.3.0) was used for quality control (QC) and preliminary analysis. Only high-quality spots with sufficient gene coverage (>=2000) were retained for downstream analysis. Like scRNA-seq data, the spatial expression data was first normalized to a log scale using the SCTransform method (v0.3.5). Top 2000 highly variable genes were then identified based on the variance of expression across spots for the principal component analysis (PCA) input. UMAP embeddings were generated for visualization at the reduced dimensionality (top 30 PCs). Spots were clustered with a shared nearest neighbor (SNN) modularity optimization-based clustering algorithm (built in Seurat). Samples were integrated and batch-effect-removed using the Harmony package (v0.1). In addition to the spatial spot view of the expression pattern, we used UMAP to visualize the expression pattern of spots associated with the identified cell types in a lower dimension using the visualization pipeline in the Seurat package. We determined each spot's potential cell type composition based on the following protocol: 1. We defined AE spots based on the k-means clustering analysis (using knowledge based key genes from different cell types). 2. For non-AE spots, we used the average expression of Krt5, Krt8, Krt17, Cldn4, and Trp53 to estimate a Krt score, and similarly, average expression of Cd8a, Cd8b1, Itgae, Trbc1, Trbc2, Sell, Ccl5, Cd69, and Cd3d for Cd8 score. We set -0.4 as cutoff for both the Cd8 and Krt score: spots with Krt/Cd8 score >-0.4 are assigned as Krt/Cd8 associated spot, and assigned blue/red color, respectively in the spatial map. In this way, a spot can be Krt spot and Cd8 spot at the same time, and we use purple color to represent this category. For a given gene list, captured the expression of relevant genes in Krt spots and AE spots and compared the distribution of the expression index. The significance of the difference was estimated by Wilcoxon rank sum test. The p-values were then $\log_{10}$ transformed and displayed as bar plot.

**Statistical analyses**

Quantitative data are presented as means ± SEM. Unpaired two-tailed Student's *t* test (two-tailed, unequal variance) was used to determine statistical significance with Prism software (GraphPad) for two-group comparison. For multiple groups, analysis of variance (ANOVA) corrected for multiple comparisons was used when appropriate (GraphPad). Log-rank (Mantel-Cox) test was used for survival curve comparison and multiple *t* test was used to analyze differences in weight loss. We considered $P < 0.05$ as significant in all statistical tests and denoted within figures as a * for each order of magnitude *P* value.

## RESULTS

### Spatial association between dysplastic epithelial progenitors and CD8$^+$ T cells is a hallmark of human PASC-PF.

We examined diseased lung sections from a cohort of PASC-PF patients that underwent lung transplantation at Cedars-Sinai Medical Center. Patients had a mean age of 52.5 years and exhibited persistent pulmonary impairment and hypoxemia, requiring oxygen supplementation **(Supplementary Table 1)**. Lung histology was notable for extensive immune cell infiltration and collagen deposition in the alveolar epithelium **(Fig. 1a).** Consistent with the observed fibrotic sequelae, we found reduced levels of AT1 and AT2 cells in PASC-PF lungs compared to controls, suggesting a persistent defect in alveolar regeneration **(Fig. 1b,c)** (39). We also observed chronic persistence of ectopic Krt5$^+$ basal cells and Krt8$^{hi}$ transitional cells in PASC-PF lungs compared to controls, which is concordant with recent reports (5, 8, 30, 40) **(Fig. 1d,e)**. PASC-PF lungs also harbored widespread expression of alpha smooth muscle actin (αSMA), indicative of myofibroblast activity in addition to pockets of Krt5$^-$ Krt17$^+$ aberrant basaloid cells previously found in IPF lungs (**Extended data Fig.1a**) (41, 42). Therefore, PASC-PF is characterized by the sustained loss of functional alveolar epithelial cells, and the persistence of dysplastic Krt5$^+$ pods and Krt8$^{hi}$ transitional cells, which is histologically akin to other fibrotic lung diseases such as idiopathic pulmonary fibrosis (IPF) (28, 29).

Previously, we reported that increased CD8$^+$ T cell levels in the bronchoalveolar lavage (BAL) fluid were associated with impaired lung function of COVID-19 convalescents (9, 10). In accordance, CD8$^+$ T cell numbers were elevated in PASC-PF patient lungs **(Fig. 1f)**. Moreover, CD8$^+$ T cell abundance was significantly higher in acute COVID-19 but not in IPF lungs when compared to controls **(Fig. 1g,h)**. Interestingly, a striking spatial association was observed between CD8$^+$ T cells, and Krt8$^{hi}$ and Krt5$^+$ areas representing dysplastic repair upon analysis of their distribution in PASC-PF lungs **(Fig. 1i,j Extended data Fig. 1b,c,h)**. Notably, this correlation between CD8$^+$ T cells, and Krt8$^{hi}$ and Krt5$^+$ dysplastic areas was unique to PASC-PF lungs but not seen in lungs from control, acute COVID-19 or IPF conditions **(Fig. 1k-m, Extended data Fig. 1d-g,i,j)**. Collectively, these data indicate that the spatiotemporal colocalization of CD8$^+$ T cells and areas of dysplastic repair is a unique feature of post-viral pulmonary fibrosis and supports immune-epithelial progenitor interactions potentially contributing to the observed defects in alveolar regeneration and chronic pulmonary sequelae.

**A mouse model of post-viral lung sequelae recapitulating features of human PASC-PF.**

To investigate the role of immune-epithelial progenitor interactions, we aimed to develop a mouse model to capture the cellular and pathological features observed in PASC-PF lungs. We used a mouse-adapted (MA-10) strain of the SARS-CoV-2 virus to productively infect WT mice. Notably, SARS-CoV-2 MA-10 infection is known to induce acute lung disease and pneumonia in mice, characterized by substantial damage to the airway epithelium, fibrin deposition, and pulmonary edema (43). Since aging is associated with an increased propensity to develop lung fibrosis post viral injury as well as severe disease after SARS-CoV-2 infection in mice, we included both young and aged mice in our study (34, 44, 45). As expected, aged C57BL/6 mice infected with SARS-CoV-2 MA-10 had increased morbidity and mortality compared to young mice **(Fig. 2a, Extended data Fig. 2a)**. Indeed, we observed marked inflammation and tissue damage acutely (at 10 days post infection (dpi)) (**Extended data Fig.2b)** (43, 46). However, irrespective of age, the majority of the lungs recovered from the acute damage and only moderate pathology primarily restricted to the subpleural regions was observed at the chronic phase (35dpi) of infection **(Fig. 2b)**.

Next, we tested SARS-CoV-2 MA-10 infection in aged BALB/c mice, which was previously reported to induce more robust inflammation and tissue sequelae compared to C57BL/6 mice (44) **(Fig. 2c, Extended data Fig. 2e)**. Consistent with the report, we observed persistent immune cell infiltration, which was largely restricted to the peri-bronchiolar regions at 35dpi **(Fig. 2d)**. However, similar to the aged C57BL/6 mice, minimal signs of collagen deposition were observed at later time points in the alveolar epithelium **(Fig. 2d)**. Consistent with what was previously reported (44) , BALB/c mice failed to maintain pulmonary $CD8^+$ T cells **(Extended data Fig. 2c,f)**, a prominent feature of human respiratory sequelae (**Fig. 1d)**. Moreover, no significant difference was observed in the development and persistence of $Krt8^{hi}$ transitional cells between aged naïve and infected (35dpi) mice in both genetic backgrounds in spite of substantial alveolar damage during acute disease **(Fig. 2e,f, Extended data Fig. 2g-i)**. Thus, SARS-CoV-2 infection in these two mouse models failed to recapitulate key features of tissue pathology and dysplastic lung repair observed in human PASC-PF.

Previously, we and others reported persistent lung inflammation and tissue pathology after influenza viral infection, particularly in aged C57BL/6 mice (9, 34, 47). Therefore, we infected young and aged WT C57BL/6 mice with influenza H1N1 A/PR8/34 strain, which causes substantial viral pneumonia and alveolar damage during acute disease (34, 48). Similar to SARS-CoV-2 infection, aged mice exhibited increased morbidity and mortality post influenza

infection **(Fig. 2g, Extended data Fig. 2j)**. In contrast to SARS-CoV-2 infection however, we observed persistent immune cell infiltration and collagen deposition in the alveolar epithelium, particularly in aged mice that persisted to 60 dpi **(Fig. 2h)**. Moreover, lungs from aged mice harbored significantly larger Krt5$^{+}$ and Krt8$^{hi}$ areas of dysplastic repair as well as higher levels of CD8$^{+}$ T cells post influenza viral pneumonia, similar to human PASC-PF lungs **(Fig. 2i, 3b,c).** Of note, we observed a sustained defect in pulmonary function in aged mice up to 60dpi following influenza viral pneumonia, mimicking the impaired lung function observed in patients with severe pulmonary sequelae after acute COVID-19 **(Fig. 2j,k)** (9, 40). The exact mechanisms underlying the divergent trajectories in recovery following acute alveolar injury due to SARS-CoV-2 MA-10 and influenza viral infections remain unclear. Nevertheless, extensive evaluation of various mouse viral pneumonia models indicates influenza infection in aged mice has closer histopathological alignment with features of chronic pulmonary sequelae observed in PASC-PF lungs and can serve as a clinically relevant model to study the mechanisms of viral infection-mediated lung fibrosis.

**Exuberant tissue CD8$^{+}$ T cell responses impair alveolar regeneration and promote dysplastic lung repair following viral pneumonia.**

To further investigate the dynamics of the induction of lung fibrosis, we infected young and aged mice with influenza virus and characterized the immune and epithelial progenitor compartments over time **(Fig 3a, Extended data Fig. 3a)**. The induction of epithelial progenitor activity was comparable in young and aged mice during the acute phase of infection (up to 14dpi) but diverged at later timepoints with increased Krt5$^{+}$ and Krt8$^{hi}$ progenitors in aged mice **(Fig. 3a-c)**. These trends correlated with a persistent age-associated defect in alveolar regeneration, exemplified by a sustained reduction in AT2 cell numbers **(Extended data Fig. 3b,c)**. Consistent with our previous study, lungs from aged mice harbored significantly higher levels of CD8$^{+}$ T cells post influenza infection compared those of young mice **(Fig. 3d)** (9, 34). Similar to human PASC-PF lungs, we also observed a spatial association between CD8$^{+}$ T cells and Krt8$^{hi}$ areas of dysplastic repair, reinforcing the relevance of this model to study chronic pulmonary sequelae (**Fig. 3e, 1i**). Furthermore, the association between CD8$^{+}$ T cells and Krt8$^{hi}$ areas was seen only at post-acute timepoints and strengthened over time, recapitulating features of human lungs after severe SARS-CoV-2 infection and suggesting these immune-epithelial progenitor interactions are primarily a feature of chronic sequelae of viral infections (**Fig. 3f**).

To understand the role of the persistent CD8$^{+}$ T cells at this stage, we treated aged influenza-infected mice with CD8$^{+}$ T cell-depleting Ab (αCD8) or isotype control Ab starting from 21dpi

**(Fig. 3g)**. This post-acute timepoint was chosen to ensure no interference with the essential antiviral activities of $CD8^+$ T cells during acute infection as the virus is completely cleared by 15 dpi in this model (34). $CD8^+$ T cell depletion improved histological evidence of disease in aged but not young mice **(Fig. 3h, Extended data Fig. 3d).** Importantly, $Krt5^+$ and $Krt8^{hi}$ areas were significantly reduced by depletion of $CD8^+$ T cells **(Fig. 3i,j),** suggesting that $CD8^+$ T cells are essential for the maintenance of dysplastic repair areas after recovery from acute disease. Interestingly, AT1 and AT2 cells were markedly increased, and the alveolar architecture was restored after $CD8^+$ T- cell depletion **(Fig. 3k,l)**. We also observed a concomitant improvement in lung function after αCD8 treatment, suggesting that exuberant $CD8^+$ T cell responses in the aftermath of acute disease affected the restoration of the alveolar spaces resulting in chronic impairment of alveolar gas-exchange function **(Fig. 3m,n).** Whether the observed decrease in $Krt5^+$ and $Krt8^{hi}$ cells post $CD8^+$ T cell depletion is a result of complete differentiation into mature alveolar cell types or apoptosis of the progenitors remains to be elucidated using lineage-tracing studies, which are logistically challenging to perform in aged mice. Moreover, since the expansion of ectopic $Krt5^+$ basal cells and $Krt8^{hi}$ transitional cells was observed in the distal lung as early as 9dpi, it is unlikely that the depletion of $CD8^+$ T cells 21dpi onwards affected the induction of the dysplastic repair program. Notably, depletion of $CD8^+$ T cells resolved $Krt5^+$ but not $Krt8^{hi}$ areas in young mice and did not dramatically affect lung pathology or alveolar regeneration (**Extended data Fig. 3d-i)**, suggesting that $CD8^+$ T cells may specifically influence age-associated dysplastic lung repair.

To dissect the roles of circulating $CD8^+$ T cells and lung resident memory $CD8^+$ T cells in impairing alveolar regeneration, we used low and high dose αCD8 treatment to deplete circulating and pulmonary $CD8^+$ T cells respectively, in aged influenza-infected mice (34, 49). We found that the resolution of areas of dysplastic repair only occurs upon depletion of pulmonary $CD8^+$ T cells but not circulating $CD8^+$ T cells **(Extended data Fig. 3j,k)** (34), suggesting that lung-resident $CD8^+$ T cells are required for the maintenance of dysplastic lung repair. Taken together, our results strongly implicate the persistent tissue $CD8^+$ T cell responses in the development of chronic pulmonary sequelae post viral pneumonia in aged animals.

**Spatial transcriptomics reveal proximal interactions between $CD8^+$ T cells, macrophages, and $Krt5^+$ and $Krt8^{hi}$-rich areas of dysplastic repair.**

Given the heterogenous distribution of tissue pathology and the importance of capturing the spatially confined interactions between immune and epithelial progenitor cells within areas of dysplastic repair, we performed spatial transcriptomics on aged influenza-infected mouse lungs

(60dpi) treated with control Ab or αCD8 **(Fig. 4a)**. Following UMAP visualization and clustering of the capture spots **(Extended data Fig. 4a,b)**, we observed a strong association between gene expression signatures of $CD8^+$ T cells, and $Krt5^+$ and $Krt8^{hi}$ areas of dysplastic repair, similar to immunostaining results **(Fig 4b, 3e)**. Consistent with previous data, gene expression signatures of $Krt5^+$ and $Krt8^{hi}$ progenitors were dramatically reduced in αCD8-treated lungs, with a concomitant increase in healthy alveolar epithelial cells **(Fig 4b, 3i-k, Extended data Fig. 4d,e)**. This also corresponded with the expression pattern of fibrosis, with the strongest enrichment within $Krt5^+$ and $Krt8^{hi}$ areas and a similar reduction in αCD8-treated lungs **(Extended data Fig. 4c)**. We further performed an agnostic evaluation of signaling pathways differentially regulated within the healthy alveolar epithelium compared to $Krt5^+$ and $Krt8^{hi}$-rich areas of dysplastic repair using Gene Set Enrichment Analysis (GSEA) **(Fig. 4c)**. Several pathways associated with inflammatory responses were highly active within areas of dysplastic repair, whereas growth factor responses and restoration of the vasculature were prominently observed in the healthy alveolar epithelium.

Upon investigation of specific gene expression-signatures, we observed an enrichment of $Krt8^{hi}$ transitional cells (also known as alveolar differentiation intermediates (22), damage-associated transitional progenitors (21), and pre-alveolar type-1 transitional cell state (20)) **(Fig. 4d)** and aberrant basaloid cells (42) **(Fig. 4e),** particularly within areas of dysplastic repair. Evaluation of various immune and epithelial cell marker signatures revealed prominent enrichment of monocyte-derived macrophages in $Krt5^+$ and $Krt8^{hi}$-rich areas in addition to other immune cells including $CD4^+$ T cells, interstitial macrophages, B-cells, and natural killer cells **(Fig. 4f, Extended data Fig. 4f,g)**. In contrast, gene expression signatures associated with pro-repair tissue-resident alveolar macrophages, AT1, and AT2 cells were primarily observed within the healthy alveolar epithelium **(Fig 4f, Extended data Fig. 4e,h)**. To further characterize the immune-epithelial progenitor niche within areas of dysplastic repair, we performed a correlation analysis and found that $CD8^+$ T cells and monocyte-derived macrophages were physically clustered around $Krt5^+$ and $Krt8^{hi}$ areas of dysplastic repair, and excluded from areas enriched with alveolar macrophages and mature alveolar epithelial cells **(Fig. 4g)**.

To validate our findings from the spatial transcriptomics data, we immunostained aged influenza-infected mouse lungs and identified a similar enrichment of $CX3CR1^+$ monocyte-derived macrophages within $Krt8^{hi}$ areas of dysplastic repair **(Fig. 4h,i)**. Interestingly, $CD8^+$ T cell depletion resulted in a decrease in $CX3CR1^+$ macrophage numbers, suggesting a potential role for their recruitment and maintenance in lungs **(Fig. 4j,k, Extended data Fig. 4g)**. Similar

to our mouse model of post-viral sequelae, human PASC-PF lungs exhibited an increase in macrophage populations compared to controls **(Fig. 4l,m)**, which were also strongly enriched within areas of dysplastic repair **(Fig. 4n,o)**. Together, our data revealed a conserved finding in both mouse and human post-viral lungs, where $CD8^+$ T cells are present in fibrotic regions and in proximity to fibroproliferative mediators such as monocyte-derived macrophages, and $Krt5^+$ and $Krt8^{hi}$ dysplastic epithelial progenitors, representing a pathological niche after acute respiratory viral infections.

**A $CD8^+$ T cell-macrophage axis induces IL-1β release to arrest AT2 trans-differentiation in the transitional cell state.**

We postulated the interactions between $CD8^+$ T cells, macrophages, and epithelial progenitors within this pathological niche generated molecular cues to create a profibrotic microenvironment. We observed an enrichment of IL-1R signaling as well as inflammasome components in $Krt5^+$ and $Krt8^{hi}$-rich areas of dysplastic repair compared to the healthy alveolar epithelium in aged influenza-infected mouse lungs at 60dpi **(Fig. 5a, Extended data Fig. 5a)**.

IL-1β has been shown to promote the expansion of transitional $Krt8^+$ cells upon bleomycin injury (21, 50). Therefore, we investigated if IL-1β mediated the development of post-viral pulmonary fibrosis. First, we found that $CD64^+$ macrophages were major producers of pro-IL-1β compared to $CD64^-$ cells in influenza-infected aged lungs **(Fig. 5b and Extended data Fig. 5b)**. Since mature IL-1β release from cells requires caspase-1 mediated pro-IL-1β cleavage (51), we examined caspase-1 activity in lung macrophages after $CD8^+$ T cell depletion. Strikingly, $CD8^+$ T cell depletion significantly reduced caspase-1 activity in lung macrophages **(Fig. 5c).** Moreover, inflammasome gene signatures were attenuated with αCD8 treatment (**Extended data Fig. 5c)**, supporting the notion that $CD8^+$ T cells persisting in the lungs post infection promote chronic inflammasome activation and IL-1β release by macrophages.

$CD8^+$ T effector and memory T cells are known express high levels of IFN-γ and TNF (52). Indeed, infected aged lungs harbor high levels of TNF **(Fig. 5d)** and IFN-γ **(Fig. 5e)** expressing $CD8^+$ T cells. To determine whether IFN-γ and TNF mediate the observed inflammasome activation, we treated aged-influenza infected mice with neutralizing antibodies towards both IFN-γ and TNF starting 21dpi and observed a decrease in caspase-1 activity **(Fig. 5f)**. As this effect was similar to αCD8-treatment **(Fig. 5c, Extended data Fig. 5c)**, we directly tested if $CD8^+$ T cell-derived IFN-γ and TNF regulated macrophage inflammation activation. We used an *in vitro* coculture of macrophages and $CD8^+$ T cells isolated from mice previously infected with

influenza (42 dpi) to assess IL-1β release **(Fig. 5g)**. Indeed, we observed $CD8^+$ T cells augmented macrophage *Il1b* mRNA expression **(Extended data Fig. 5d),** caspase-1 activity **(Fig. 5h, Extended data Fig. 5e),** and IL-1β release **(Fig. 5i).** The synergistic activity between macrophages and $CD8^+$ T cells to produce IL-1β *in vitro* was not observed when isolated from naïve mice, suggesting that prior infection is necessary to prime the cells **(Extended data Fig. 5f)**. Moreover, IL-1β released into the supernatant was significantly reduced upon treatment with IFN-γ and TNF neutralizing Ab in the coculture system, confirming the role of IFN-γ and TNF in promoting IL-1β release by macrophages **(Fig. 5j)**. Consistently, we observed a similar decrease in BAL fluid IL-1β levels following treatment with either αCD8, or αIFN-γ + αTNF treatment **(Fig. 5k,l)**.

Since $CD8^+$ T cells, monocyte-derived macrophages, and $Krt8^{hi}$ progenitors accumulate within dysplastic areas after influenza infection, we tested whether macrophage-derived IL-1β is a negative regulator of AT2 to AT1 trans-differentiation. Using a 2D primary AT2 cell culture model known to induce spontaneous differentiation into AT1 cells through the transitional cell stage, we examined if conditioned media from cocultured $CD8^+$ T cells and macrophages influenced AT2 trans-differentiation **(Fig. 5m)** (18, 37). AT1 cell marker expression was reduced upon exposure to conditioned media from $CD8^+$ T cell-macrophage coculture compared to macrophages alone, which was rescued upon treatment with αIL-1β **(Fig. 5n)**. In contrast, transitional cell marker expression exhibited the opposite pattern, with increased levels within the coculture group and a dramatic reduction following αIL-1β treatment **(Fig. 5o)**. Conversely, rIL-1β treatment inhibited AT1 marker expression and promoted the expression transitional cell markers akin to previous reports (21). Collectively, our results suggest that exuberant $CD8^+$ T cell-macrophage interactions promote chronic IL-1β release to inhibit AT2 cell trans-differentiation by arresting the cells in the transitional state.

**Therapeutic neutralization of IFN-γ and TNF, or IL-1β activity enhances alveolar regeneration and restores lung function.**

Our data thus far indicate a pathological role for $CD8^+$ T cells persisting in human PASC-PF or virus-induced lung sequelae in an animal model in the development of chronic pulmonary sequelae. Since depletion of $CD8^+$ T cells is not a clinically feasible treatment strategy, we explored the therapeutic efficacy of neutralizing the cytokines that are effectors of the profibrotic $CD8^+$ T-cell. As expected, blocking IFN-γ and TNF activity in aged influenza-infected mice ameliorated fibrotic sequelae when compared to isotype controls **(Fig. 6a,b)**. Moreover, IFN-γ and TNF neutralization attenuated $Krt5^+$ and $Krt8^{hi}$ areas of dysplastic repair **(Fig. 6c,d)**,

enhanced alveolar regeneration as evidenced by the increased numbers of AT1 and AT2 cells **(Fig. 6c,e)**. The observed cellular changes also reflected in physiological benefit, with improved lung function following treatment **(Fig. 6f)**.

Next, we tested the efficacy of neutralizing IL-1β in influenza-infected aged mice and observed dramatic attenuation of lung fibrosis, which phenocopies the results of $CD8^+$ T cell depletion, and neutralization of IFN-γ and TNF **(Fig. 6g,h, Extended data Fig. 6a,b)**. Improved alveolar regeneration was also observed, as evidenced by reduced $Krt5^+$ and $Krt8^{hi}$ areas and increased AT1 and AT2 cells **(Fig. 6i-l)**. Further confirming the therapeutic efficacy of IL-1β blockade post infection, we found improved lung function in Ab-treated mice **(Fig. 6m)**. Notably, improved outcomes following IL-1β neutralization were only seen in aged mice but not young mice, which is likely due to the elevation of IL-1β observed exclusively in aged mice (**Extended data Fig. 6c,d).** Thus, these data suggest that neutralization of IFN-γ and TNF, or IL-1β in the post-acute stage of viral infection may serve as viable therapeutic options to augment alveolar regeneration and dampen fibrotic sequelae observed following respiratory viral infections (**Extended data Fig. 7**). Consistent with the observed improvement in outcomes and a recent study identifying increased BAL IL-1β levels in respiratory PASC (7), we found that circulating IL-1β levels were elevated in individuals exhibiting persistent abnormal pulmonary function compared to those that had fully recovered **(Fig. 6n),** suggesting that chronic IL-1β activity may impede the restoration of normal lung function after acute SARS-CoV-2 infection**.**

## DISCUSSION

Recent efforts have revealed several histopathological features conserved across various cohorts of respiratory PASC and PASC-PF patients including the prolonged reduction in alveolar epithelial cells (39), maintenance of Krt8$^{hi}$ and Krt5$^{+}$ dysplastic progenitors (5, 8), and the persistence of various immune cell populations in the lungs (9, 10, 53). Although immune-derived cues have recently been shown to influence lung repair (11, 21, 48, 50, 54), their exact interactions, if any, with the alveolar epithelium and role in post-viral fibrosis remain unexplored. Here, we link these independent observations in PASC-PF lungs and an animal model of post-viral fibrosis to describe spatially defined microenvironments composed of a dysregulated immune-epithelial progenitor niche that underlie dysplastic lung repair and tissue fibrosis after acute COVID-19. Intriguingly, these niches were observed specifically in PASC-PF lungs but not in acute COVD-19 or IPF lungs, indicating that these interactions are a unique feature of post-viral fibrosis.

Understanding the mechanistic basis of respiratory PASC requires suitable animal models, however, SARS-CoV-2 MA-10 infection of neither C57BL/6 nor BALB/c mice resulted in severe alveolar pathology and fibrosis beyond acute disease. Although previous studies indicate that aged BALB/c mice develop significant pulmonary inflammation and prolonged pathology after SARS-CoV-2 infection (55), our data suggest these murine SARS-CoV-2 infection models may not fully recapitulate the pathophysiology leading to PASC-PF in humans. A major deficiency of the SARS-CoV-2 mouse infection model is the absence of persistent Krt8$^{hi}$ and Krt5$^{+}$ areas – a hallmark of human PASC-PF. Moreover, CD8$^{+}$ T cells, which are enriched in human PASC-PF lungs to potentially promote the maintenance of Krt8$^{hi}$ and Krt5$^{+}$ dysplastic areas, are not appreciably increased post SARS-CoV-2 infection in BALB/c mice (9), which may be a reflection of a genetically programmed bias towards $T_{H2}$ responses (56). Thus, it is imperative to develop clinically relevant animal models of SARS-CoV-2 post-viral fibrosis, validated by comparative analyses with human PASC, to uncover the underlying mechanisms and identify therapeutic targets. Nevertheless, in this study we show that influenza infection in aged C57BL/6 mice induced chronic pulmonary sequelae that faithfully recapitulate the immunopathological features of human PASC-PF lungs.

Excessive infiltration and accumulation of profibrotic monocyte derived macrophages has been reported in the context of severe acute COVID-19, IPF, and PASC (12, 53, 57, 58). Here, we

elucidate a previously unknown role for pulmonary $CD8^+$ T cells in impaired recovery and fibrotic remodeling in PASC-PF but not acute COVID-19 or IPF lungs. This distinction is likely the product of a dysregulated and protracted antiviral response, originally aimed towards the clearance of the virus and virus-infected cells. Following viral infection-mediated alveolar injury, lung resident $CD8^+$ T cells are recruited and maintained at sites of severe damage in order to protect these vulnerable sites in case of reinfection – previously termed as repair associated memory depots (59). These pulmonary $CD8^+$ T cells typically gradually contract with successful alveolar regeneration in individuals that successfully recover from acute COVID-19 (9). However, long-term persistence of $CD8^+$ T cells in human PASC, and aged influenza-infected mice impairs lung recovery post infection and drives the development of fibrotic disease. Given the overlap in fibrogenic pathways, it has been proposed that PASC-PF may represent an intermediate state prior to potential progression towards IPF (8, 60). Whether $CD8^+$ T cells primarily dictate the balance between functional recovery and PASC-PF post infection, or also play a pivotal role in the development of IPF is an open question (61). It is also currently unclear if the prolonged maintenance and activity of $CD8^+$ T cells in lungs is a result of excessive TGF-β signaling reported to occur in PASC (8), chronic persistence of viral remnants (62, 63), or other independent mechanisms.

By combining imaging and spatial transcriptomics modalities, we show that respiratory sequelae post viral infections is, at least in part, a result of chronic IL-1β signaling downstream of aberrant interactions between $CD8^+$ T cells and monocyte-derived macrophages, mediated by IFN-γ and TNF. Although chronic IL-1β was found to impair AT2 trans-differentiation *in vitro*, the use of aged mice in our experiments posed a logistical challenge to directly test the effect of IL-1β on $Krt8^{hi}$ and $Krt5^+$ progenitors *in vivo* using transgenic mice. Thus, there exists a distinct possibility for IFN-γ and TNF as well as IL-1β and relevant downstream mediators to influence epithelial progenitor cell fate through their actions on other lung immune and non-immune cells to ultimately result in fibrotic remodeling. Nevertheless, we show that neutralization of IFN-γ and TNF, or IL-1β activity in the post-acute phase of infection can augment alveolar regeneration and dampen fibrotic sequelae. Given the observed benefits in adults and pediatric patients hospitalized with acute COVID-19, United States Food and Drug Administration has already granted emergency use authorization to the IL-1 receptor antagonist, Anakinra and the JAK-inhibitor, Baricitinib, in acute COVID-19. Our data strongly suggest that these drugs may also serve as promising candidates to treat ongoing respiratory PASC in the clinic.

**Acknowledgements**

We thank the Lung Institute BioBank study staff at Cedars-Sinai Medical Center for providing human lung specimens and patients' clinical data. We thank Drs. Vaughan and Zemans for protocols to isolate and culture AT2 cells. Schematics in the manuscript were created with BioRender.com. Data for this manuscript were generated using the Flow Cytometry and Research Histology Core Facilities at the University of Virginia. 10X Visium spatial transcriptomics on mouse tissues was performed in the Advanced Genomics Core at the University of Michigan.

The study was in part supported by the US National Institutes of Health grants AI147394, AG069264, AI112844, HL170961, AI176171 and AI154598 to J.S, R01HL132287, R01HL167202, and R01HL132177 to Y.M.S, and F31HL170746 and T32AI007496 to H.N.

**Author contribution**

H.N. & J.S. conceived the overall project. H.N. I.S.C., W.Q., S.H., T. P., C.Z., P.C., and J.S. designed the experimental strategy and analyzed data. C.L., N.G., Y.W., X.W., Y.M.S., E.F, G.S., J.T., C.Y., L.M., G.C., A.K., A.C., P.P., Y.M.S., and J.W., performed experiments, analyzed data, or contributed critical reagents to the study. H.N. & J.S. wrote the original draft. All authors read, edited, and approved the final manuscript.

## REFERENCES


1. Nalbandian A, Sehgal K, Gupta A, Madhavan MV, McGroder C, Stevens JS, et al. Post-acute COVID-19 syndrome. Nature Medicine. 2021;27(4):601-15.
2. Al-Aly Z, Xie Y, Bowe B. High-dimensional characterization of post-acute sequelae of COVID-19. Nature. 2021;594(7862):259-64.
3. Littlefield KM, Watson RO, Schneider JM, Neff CP, Yamada E, Zhang M, et al. SARS-CoV-2-specific T cells associate with inflammation and reduced lung function in pulmonary post-acute sequalae of SARS-CoV-2. PLOS Pathogens. 2022;18(5):e1010359.
4. Bowe B, Xie Y, Al-Aly Z. Postacute sequelae of COVID-19 at 2 years. Nature Medicine. 2023.
5. Jyothula SSK, Peters A, Liang Y, Bi W, Shivshankar P, Yau S, et al. Fulminant lung fibrosis in non-resolvable COVID-19 requiring transplantation. eBioMedicine. 2022;86.
6. Stewart I, Jacob J, George PM, Molyneaux PL, Porter JC, Allen RJ, et al. Residual Lung Abnormalities after COVID-19 Hospitalization: Interim Analysis of the UKILD Post–COVID-19 Study. American Journal of Respiratory and Critical Care Medicine. 2022;207(6):693-703.
7. Gagiannis D, Hackenbroch C, Bloch W, Zech F, Kirchhoff F, Djudjaj S, et al. Clinical, Imaging, and Histopathological Features of Pulmonary Sequelae after Mild COVID-19. American Journal of Respiratory and Critical Care Medicine. 2023;208(5):618-21.
8. Yao C, Parimon T, Espindola MS, Hohmann MS, Konda B, Hogaboam CM, et al. Maladaptive TGF-β Signals to the Alveolar Epithelium Drive Fibrosis after COVID-19 Infection. Am J Respir Crit Care Med. 2023;208(2):201-4.
9. Cheon IS, Li C, Son YM, Goplen NP, Wu Y, Cassmann T, et al. Immune signatures underlying post-acute COVID-19 lung sequelae. Science Immunology.6(65):eabk1741.
10. Vijayakumar B, Boustani K, Ogger PP, Papadaki A, Tonkin J, Orton CM, et al. Immuno-proteomic profiling reveals aberrant immune cell regulation in the airways of individuals with ongoing post-COVID-19 respiratory disease. Immunity. 2022;55(3):542-56.e5.
11. Narasimhan H, Wu Y, Goplen NP, Sun J. Immune determinants of chronic sequelae after respiratory viral infection. Science Immunology.7(73):eabm7996.
12. Phetsouphanh C, Darley DR, Wilson DB, Howe A, Munier CML, Patel SK, et al. Immunological dysfunction persists for 8 months following initial mild-to-moderate SARS-CoV-2 infection. Nature Immunology. 2022;23(2):210-6.
13. Merad M, Blish CA, Sallusto F, Iwasaki A. The immunology and immunopathology of COVID-19. Science. 2022;375(6585):1122-7.
14. Arish M, Qian W, Narasimhan H, Sun J. COVID-19 immunopathology: From acute diseases to chronic sequelae. Journal of Medical Virology. 2023;95(1):e28122.
15. Adam D, Perotin JM, Lebargy F, Birembaut P, Deslée G, Coraux C. Régénération de l'épithélium des voies aériennes. Revue des Maladies Respiratoires. 2014;31(4):300-11.
16. Grace CB, Lyndsey MM, Chaofan L, Yong H, Daniel A, Imre N, et al. Reduction in circulating monocytes correlates with persistent post-COVID pulmonary fibrosis in multi-omic comparison of long-haul COVID and IPF. medRxiv. 2022:2022.09.30.22280468.
17. Barkauskas CE, Cronce MJ, Rackley CR, Bowie EJ, Keene DR, Stripp BR, et al. Type 2 alveolar cells are stem cells in adult lung. J Clin Invest. 2013;123(7):3025-36.
18. Nabhan AN, Brownfield DG, Harbury PB, Krasnow MA, Desai TJ. Single-cell Wnt signaling niches maintain stemness of alveolar type 2 cells. Science. 2018;359(6380):1118-23.
19. Zacharias WJ, Frank DB, Zepp JA, Morley MP, Alkhaleel FA, Kong J, et al. Regeneration of the lung alveolus by an evolutionarily conserved epithelial progenitor. Nature. 2018;555(7695):251-5.

20. Kobayashi Y, Tata A, Konkimalla A, Katsura H, Lee RF, Ou J, et al. Persistence of a regeneration-associated, transitional alveolar epithelial cell state in pulmonary fibrosis. Nature Cell Biology. 2020;22(8):934-46.
21. Choi J, Park JE, Tsagkogeorga G, Yanagita M, Koo BK, Han N, et al. Inflammatory Signals Induce AT2 Cell-Derived Damage-Associated Transient Progenitors that Mediate Alveolar Regeneration. Cell Stem Cell. 2020;27(3):366-82.e7.
22. Strunz M, Simon LM, Ansari M, Kathiriya JJ, Angelidis I, Mayr CH, et al. Alveolar regeneration through a Krt8+ transitional stem cell state that persists in human lung fibrosis. Nature Communications. 2020;11(1):3559.
23. Vaughan AE, Brumwell AN, Xi Y, Gotts JE, Brownfield DG, Treutlein B, et al. Lineage-negative progenitors mobilize to regenerate lung epithelium after major injury. Nature. 2015;517(7536):621-5.
24. Kumar PA, Hu Y, Yamamoto Y, Hoe NB, Wei TS, Mu D, et al. Distal airway stem cells yield alveoli in vitro and during lung regeneration following H1N1 influenza infection. Cell. 2011;147(3):525-38.
25. Zuo W, Zhang T, Wu DZ, Guan SP, Liew AA, Yamamoto Y, et al. p63(+)Krt5(+) distal airway stem cells are essential for lung regeneration. Nature. 2015;517(7536):616-20.
26. Weiner AI, Zhao G, Zayas HM, Holcomb NP, Adams-Tzivelekidis S, Wong J, et al. ΔNp63 drives dysplastic alveolar remodeling and restricts epithelial plasticity upon severe lung injury. Cell Rep. 2022;41(11):111805.
27. Xi Y, Kim T, Brumwell AN, Driver IH, Wei Y, Tan V, et al. Local lung hypoxia determines epithelial fate decisions during alveolar regeneration. Nature Cell Biology. 2017;19(8):904-14.
28. Xie T, Lynn H, Parks WC, Stripp B, Chen P, Jiang D, et al. Abnormal respiratory progenitors in fibrotic lung injury. Stem Cell Research & Therapy. 2022;13(1):64.
29. Jiang P, Gil de Rubio R, Hrycaj SM, Gurczynski SJ, Riemondy KA, Moore BB, et al. Ineffectual Type 2–to–Type 1 Alveolar Epithelial Cell Differentiation in Idiopathic Pulmonary Fibrosis: Persistence of the KRT8hi Transitional State. American Journal of Respiratory and Critical Care Medicine. 2020;201(11):1443-7.
30. Parimon T, Espindola M, Marchevsky A, Rampolla R, Chen P, Hogaboam CM. Potential mechanisms for lung fibrosis associated with COVID-19 infection. Qjm. 2023;116(7):487-92.
31. Melms JC, Biermann J, Huang H, Wang Y, Nair A, Tagore S, et al. A molecular single-cell lung atlas of lethal COVID-19. Nature. 2021;595(7865):114-9.
32. Fang Y, Liu H, Huang H, Li H, Saqi A, Qiang L, et al. Distinct stem/progenitor cells proliferate to regenerate the trachea, intrapulmonary airways and alveoli in COVID-19 patients. Cell Research. 2020;30(8):705-7.
33. Kathiriya JJ, Wang C, Zhou M, Brumwell A, Cassandras M, Le Saux CJ, et al. Human alveolar type 2 epithelium transdifferentiates into metaplastic KRT5(+) basal cells. Nat Cell Biol. 2022;24(1):10-23.
34. Goplen NP, Wu Y, Son YM, Li C, Wang Z, Cheon IS, et al. Tissue-resident CD8(+) T cells drive age-associated chronic lung sequelae after viral pneumonia. Sci Immunol. 2020;5(53).
35. Goplen N, Karim MZ, Liang Q, Gorska MM, Rozario S, Guo L, et al. Combined sensitization of mice to extracts of dust mite, ragweed, and Aspergillus species breaks through tolerance and establishes chronic features of asthma. Journal of Allergy and Clinical Immunology. 2009;123(4):925-32.e11.
36. Major J, Crotta S, Finsterbusch K, Chakravarty P, Shah K, Frederico B, et al. Endothelial AHR activity prevents lung barrier disruption in viral infection. Nature. 2023.
37. Riemondy KA, Jansing NL, Jiang P, Redente EF, Gillen AE, Fu R, et al. Single cell RNA sequencing identifies TGFβ as a key regenerative cue following LPS-induced lung injury. JCI Insight. 2019;5(8).
38. Huang S, Zhu B, Cheon IS, Goplen NP, Jiang L, Zhang R, et al. PPAR-γ in Macrophages Limits Pulmonary Inflammation and Promotes Host Recovery following Respiratory Viral Infection. Journal of virology. 2019;93(9):e00030-19.

39. Rendeiro AF, Ravichandran H, Kim J, Borczuk AC, Elemento O, Schwartz RE. Persistent alveolar type 2 dysfunction and lung structural derangement in post-acute COVID-19. medRxiv. 2022.
40. Bharat A, Querrey M, Markov NS, Kim S, Kurihara C, Garza-Castillon R, et al. Lung transplantation for patients with severe COVID-19. Science Translational Medicine. 2020;12(574):eabe4282.
41. Habermann AC, Gutierrez AJ, Bui LT, Yahn SL, Winters NI, Calvi CL, et al. Single-cell RNA sequencing reveals profibrotic roles of distinct epithelial and mesenchymal lineages in pulmonary fibrosis. Sci Adv. 2020;6(28):eaba1972.
42. Adams TS, Schupp JC, Poli S, Ayaub EA, Neumark N, Ahangari F, et al. Single-cell RNA-seq reveals ectopic and aberrant lung-resident cell populations in idiopathic pulmonary fibrosis. Sci Adv.6(28):eaba1983.
43. Leist SR, Dinnon KH, 3rd, Schäfer A, Tse LV, Okuda K, Hou YJ, et al. A Mouse-Adapted SARS-CoV-2 Induces Acute Lung Injury and Mortality in Standard Laboratory Mice. Cell. 2020;183(4):1070-85.e12.
44. Dinnon KH, Leist SR, Okuda K, Dang H, Fritch EJ, Gully KL, et al. SARS-CoV-2 infection produces chronic pulmonary epithelial and immune cell dysfunction with fibrosis in mice. Science Translational Medicine.14(664):eabo5070.
45. Caporarello N, Meridew JA, Aravamudhan A, Jones DL, Austin SA, Pham TX, et al. Vascular dysfunction in aged mice contributes to persistent lung fibrosis. Aging Cell. 2020;19(8):e13196.
46. Dinnon KH, Leist SR, Schäfer A, Edwards CE, Martinez DR, Montgomery SA, et al. A mouse-adapted model of SARS-CoV-2 to test COVID-19 countermeasures. Nature. 2020;586(7830):560-6.
47. Cookenham T, Lanzer KG, Tighe M, Ward JM, Reiley WW, Blackman MA. Visualization of Resident Memory CD8 T Cells in the Lungs of Young and Aged Influenza Memory Mice and after Heterosubtypic Challenge. ImmunoHorizons. 2021;5(7):543-56.
48. Wei X, Narasimhan H, Zhu B, Sun J. Host Recovery from Respiratory Viral Infection. Annual Review of Immunology. 2023;41(1):277-300.
49. Schenkel JM, Fraser KA, Beura LK, Pauken KE, Vezys V, Masopust D. T cell memory. Resident memory CD8 T cells trigger protective innate and adaptive immune responses. Science. 2014;346(6205):98-101.
50. Katsura H, Kobayashi Y, Tata PR, Hogan BLM. IL-1 and TNFα Contribute to the Inflammatory Niche to Enhance Alveolar Regeneration. Stem Cell Reports. 2019;12(4):657-66.
51. Thornberry NA, Lazebnik Y. Caspases: Enemies Within. Science. 1998;281(5381):1312-6.
52. Kaech SM, Ahmed R. Memory CD8+ T cell differentiation: initial antigen encounter triggers a developmental program in naïve cells. Nat Immunol. 2001;2(5):415-22.
53. Joseph IB, Connor HP, Karolina JS, Nikolay SM, Estefani D, Emmy J, et al. Expansion of profibrotic monocyte-derived alveolar macrophages in patients with persistent respiratory symptoms and radiographic abnormalities after COVID-19. bioRxiv. 2023:2023.07.30.551145.
54. Choi J, Jang YJ, Dabrowska C, Iich E, Evans KV, Hall H, et al. Release of Notch activity coordinated by IL-1β signalling confers differentiation plasticity of airway progenitors via Fosl2 during alveolar regeneration. Nat Cell Biol. 2021;23(9):953-66.
55. Dinnon KH, Leist SR, Okuda K, Dang H, Fritch EJ, Gully KL, et al. A model of persistent post SARS-CoV-2 induced lung disease for target identification and testing of therapeutic strategies. bioRxiv. 2022:2022.02.15.480515.
56. Reiner SL, Locksley RM. The regulation of immunity to Leishmania major. Annu Rev Immunol. 1995;13:151-77.
57. Wendisch D, Dietrich O, Mari T, von Stillfried S, Ibarra IL, Mittermaier M, et al. SARS-CoV-2 infection triggers profibrotic macrophage responses and lung fibrosis. Cell. 2021;184(26):6243-61.e27.
58. Misharin AV, Morales-Nebreda L, Reyfman PA, Cuda CM, Walter JM, McQuattie-Pimentel AC, et al. Monocyte-derived alveolar macrophages drive lung fibrosis and persist in the lung over the life span. Journal of Experimental Medicine. 2017;214(8):2387-404.

59. Takamura S, Yagi H, Hakata Y, Motozono C, McMaster SR, Masumoto T, et al. Specific niches for lung-resident memory CD8+ T cells at the site of tissue regeneration enable CD69-independent maintenance. Journal of Experimental Medicine. 2016;213(13):3057-73.
60. Parimon T, Espindola M, Marchevsky A, Rampolla R, Chen P, Hogaboam CM. Potential mechanisms for lung fibrosis associated with COVID-19 infection. QJM: An International Journal of Medicine. 2022:hcac206.
61. Wang Z, Wang S, Goplen Nick P, Li C, Cheon In S, Dai Q, et al. PD-1hi CD8+ resident memory T cells balance immunity and fibrotic sequelae. Science Immunology. 2019;4(36):eaaw1217.
62. Chen B, Julg B, Mohandas S, Bradfute SB, Force RMPT. Viral persistence, reactivation, and mechanisms of long COVID. eLife. 2023;12:e86015.
63. Proal AD, VanElzakker MB, Aleman S, Bach K, Boribong BP, Buggert M, et al. SARS-CoV-2 reservoir in post-acute sequelae of COVID-19 (PASC). Nature Immunology. 2023.

Fig.1

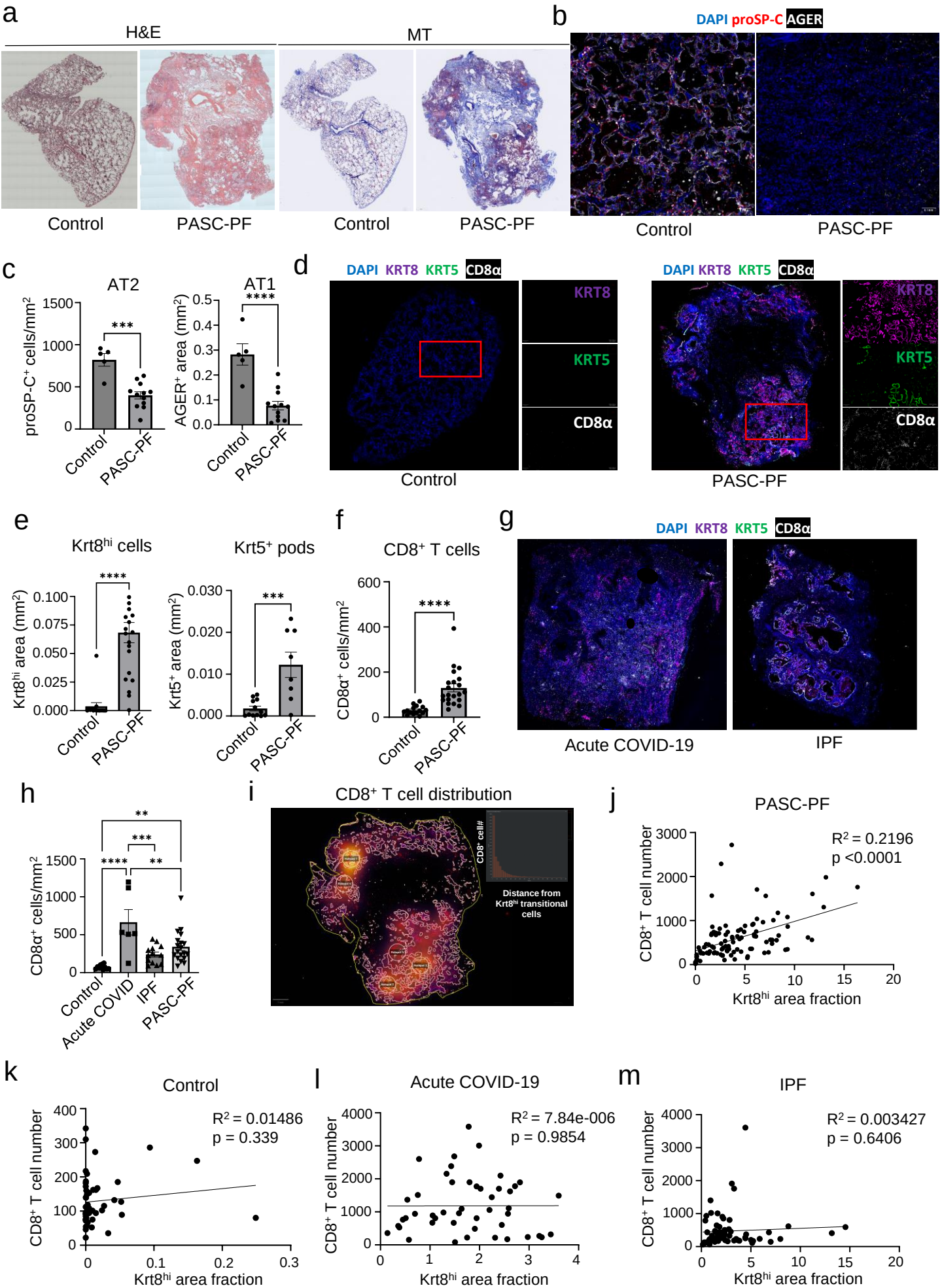
a
H&E
MT
Control
PASC-PF
Control
PASC-PF
b
DAPI proSP-C AGER
Control
PASC-PF
c
AT2
proSP-C⁺ cells/mm²
1500
1000
500
0
***
Control
PASC-PF
AT1
AGER⁺ area (mm²)
0.5
0.4
0.3
0.2
0.1
0.0
****
Control
PASC-PF
d
DAPI KRT8 KRT5 CD8α
KRT8
KRT5
CD8α
Control
DAPI KRT8 KRT5 CD8α
KRT8
KRT5
CD8α
PASC-PF
e
Krt8hi cells
Krt8hi area (mm²)
0.100
0.075
0.050
0.025
0.000
****
Control
PASC-PF
Krt5⁺ pods
Krt5⁺ area (mm²)
0.030
0.020
0.010
0.000
***
Control
PASC-PF
f
CD8⁺ T cells
CD8α⁺ cells/mm²
600
400
200
0
****
Control
PASC-PF
g
DAPI KRT8 KRT5 CD8α
Acute COVID-19
IPF
h
CD8α⁺ cells/mm²
1500
1000
500
0
**
***
****
**
Control
Acute COVID
IPF
PASC-PF
i
CD8⁺ T cell distribution
CD8⁺ cell#
Distance from Krt8hi transitional cells
j
PASC-PF
R² = 0.2196
p <0.0001
CD8⁺ T cell number
3000
2000
1000
0
0
5
10
15
20
Krt8hi area fraction
k
Control
R² = 0.01486
p = 0.339
CD8⁺ T cell number
400
300
200
100
0
0
0.1
0.2
0.3
Krt8hi area fraction
l
Acute COVID-19
R² = 7.84e-006
p = 0.9854
CD8⁺ T cell number
4000
3000
2000
1000
0
0
1
2
3
4
Krt8hi area fraction
m
IPF
R² = 0.003427
p = 0.6406
CD8⁺ T cell number
4000
3000
2000
1000
0
0
5
10
15
20
Krt8hi area fraction

# Fig.2

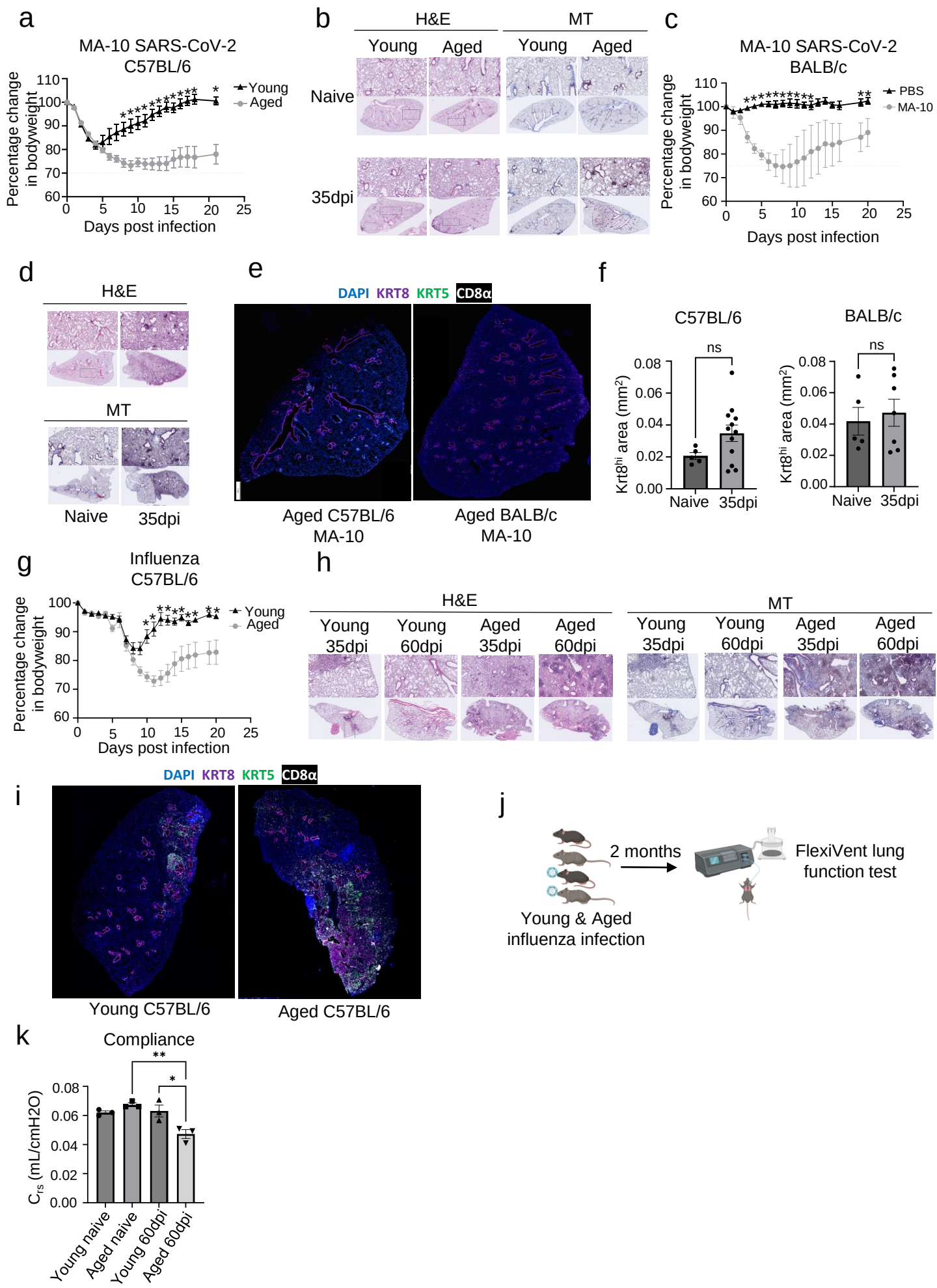
a
MA-10 SARS-CoV-2
C57BL/6
Percentage change in bodyweight
Days post infection
Young
Aged
b
H&E
MT
Young
Aged
Naive
35dpi
c
MA-10 SARS-CoV-2
BALB/c
PBS
MA-10
d
H&E
MT
Naive
35dpi
e
DAPI KRT8 KRT5 CD8α
Aged C57BL/6
MA-10
Aged BALB/c
MA-10
f
C57BL/6
BALB/c
ns
Krt8hi area (mm2)
Naive
35dpi
g
Influenza
C57BL/6
h
Young 35dpi
Young 60dpi
Aged 35dpi
Aged 60dpi
i
Young C57BL/6
Aged C57BL/6
j
2 months
FlexiVent lung function test
Young & Aged influenza infection
k
Compliance
Crs (mL/cmH2O)
Young naive
Aged naive
Young 60dpi
Aged 60dpi

Fig.3

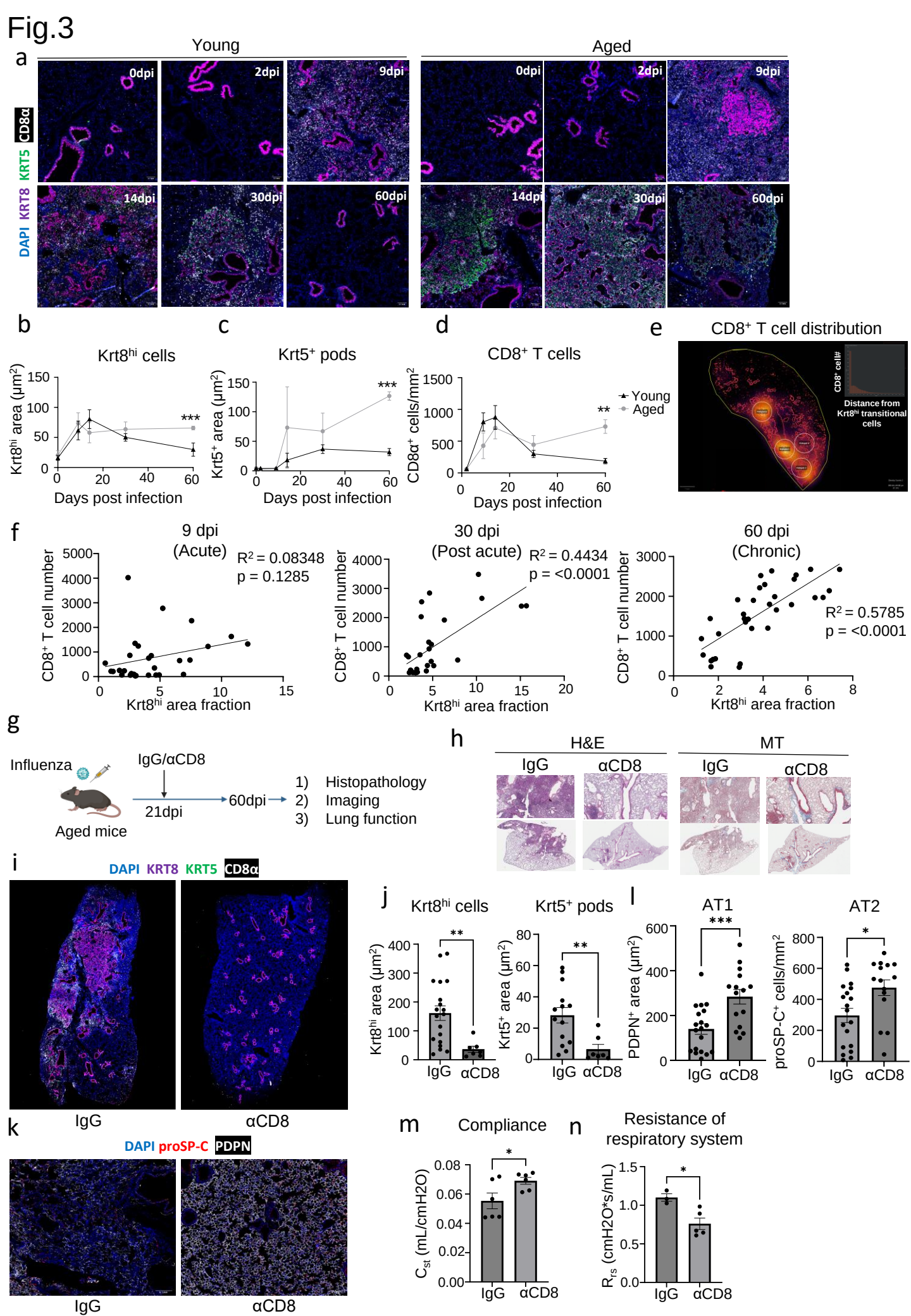
a
Young
Aged
0dpi
2dpi
9dpi
14dpi
30dpi
60dpi
CD8α
KRT5
KRT8
DAPI
b
Krt8hi cells
Krt8hi area (μm2)
Days post infection
c
Krt5+ pods
Krt5+ area (μm2)
Days post infection
d
CD8+ T cells
CD8α+ cells/mm2
Days post infection
Young
Aged
e
CD8+ T cell distribution
CD8+ cell#
Distance from Krt8hi transitional cells
f
9 dpi (Acute)
R2 = 0.08348
p = 0.1285
30 dpi (Post acute)
R2 = 0.4434
p = <0.0001
60 dpi (Chronic)
R2 = 0.5785
p = <0.0001
CD8+ T cell number
Krt8hi area fraction
g
Influenza
Aged mice
IgG/αCD8
21dpi
60dpi
1) Histopathology
2) Imaging
3) Lung function
h
H&E
MT
IgG
αCD8
i
DAPI KRT8 KRT5 CD8α
IgG
αCD8
j
Krt8hi cells
Krt5+ pods
Krt8hi area (μm2)
Krt5+ area (μm2)
IgG
αCD8
l
AT1
AT2
PDPN+ area (μm2)
proSP-C+ cells/mm2
IgG
αCD8
k
DAPI proSP-C PDPN
IgG
αCD8
m
Compliance
Cst (mL/cmH2O)
IgG
αCD8
n
Resistance of respiratory system
Rrs (cmH2O*s/mL)
IgG
αCD8

# Fig. 4

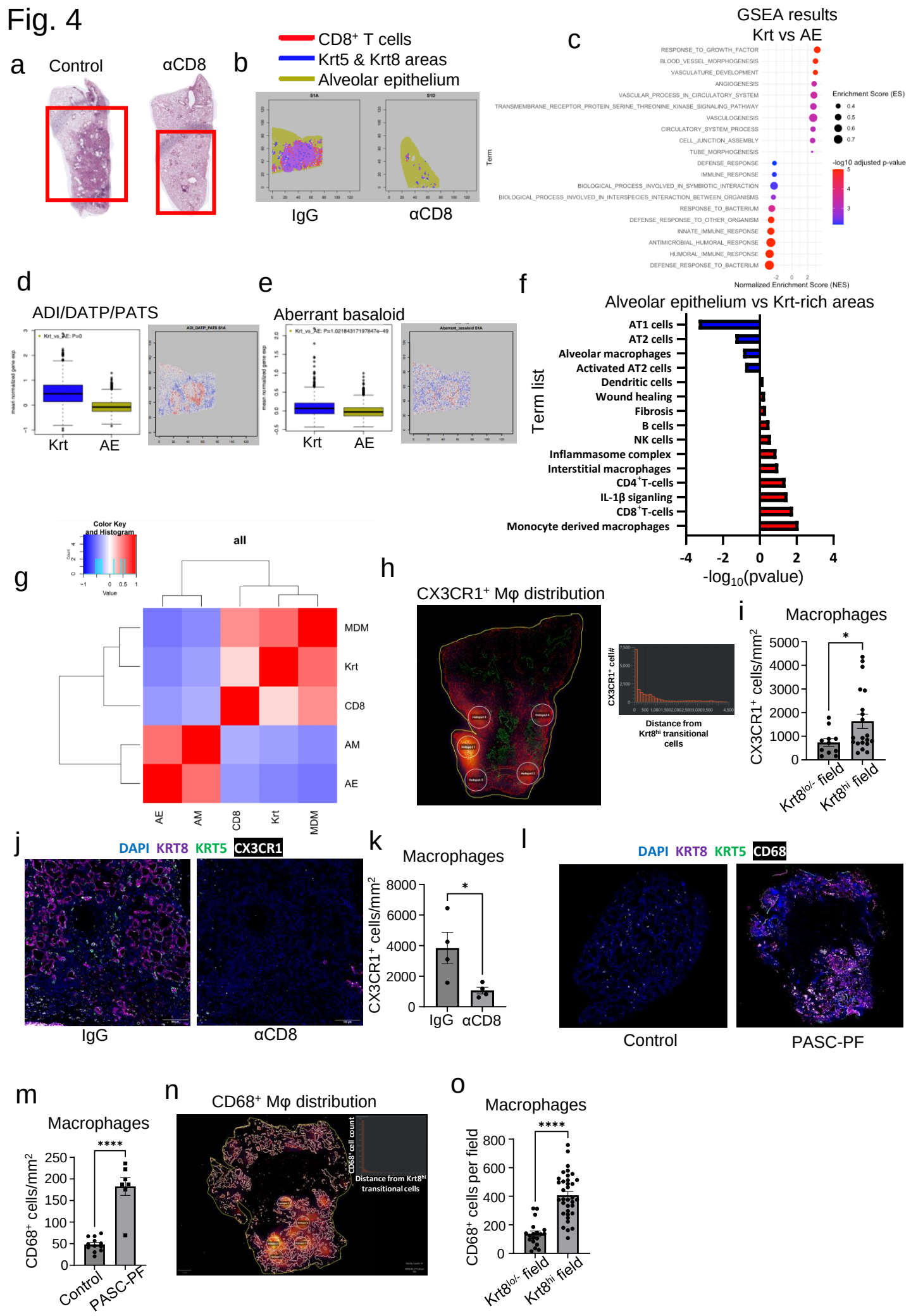
a
Control
αCD8
b
CD8+ T cells
Krt5 & Krt8 areas
Alveolar epithelium
S1A
S1D
IgG
αCD8
c
GSEA results
Krt vs AE
RESPONSE_TO_GROWTH_FACTOR
BLOOD_VESSEL_MORPHOGENESIS
VASCULATURE_DEVELOPMENT
ANGIOGENESIS
VASCULAR_PROCESS_IN_CIRCULATORY_SYSTEM
TRANSMEMBRANE_RECEPTOR_PROTEIN_SERINE_THREONINE_KINASE_SIGNALING_PATHWAY
VASCULOGENESIS
CIRCULATORY_SYSTEM_PROCESS
CELL_JUNCTION_ASSEMBLY
TUBE_MORPHOGENESIS
DEFENSE_RESPONSE
IMMUNE_RESPONSE
BIOLOGICAL_PROCESS_INVOLVED_IN_SYMBIOTIC_INTERACTION
BIOLOGICAL_PROCESS_INVOLVED_IN_INTERSPECIES_INTERACTION_BETWEEN_ORGANISMS
RESPONSE_TO_BACTERIUM
DEFENSE_RESPONSE_TO_OTHER_ORGANISM
INNATE_IMMUNE_RESPONSE
ANTIMICROBIAL_HUMORAL_RESPONSE
HUMORAL_IMMUNE_RESPONSE
DEFENSE_RESPONSE_TO_BACTERIUM
Term
Enrichment Score (ES)
0.4
0.5
0.6
0.7
-log10 adjusted p-value
Normalized Enrichment Score (NES)
d
ADI/DATP/PATS
Krt
AE
e
Aberrant basaloid
Krt
AE
f
Alveolar epithelium vs Krt-rich areas
Term list
AT1 cells
AT2 cells
Alveolar macrophages
Activated AT2 cells
Dendritic cells
Wound healing
Fibrosis
B cells
NK cells
Inflammasome complex
Interstitial macrophages
CD4+T-cells
IL-1β siganling
CD8+T-cells
Monocyte derived macrophages
-log10(pvalue)
g
Color Key and Histogram
Value
all
MDM
Krt
CD8
AM
AE
h
CX3CR1+ Mφ distribution
CX3CR1+ cell#
Distance from Krt8hi transitional cells
i
Macrophages
CX3CR1+ cells/mm2
Krt8lo/- field
Krt8hi field
j
DAPI KRT8 KRT5 CX3CR1
IgG
αCD8
k
Macrophages
CX3CR1+ cells/mm2
IgG
αCD8
l
DAPI KRT8 KRT5 CD68
Control
PASC-PF
m
Macrophages
CD68+ cells/mm2
Control
PASC-PF
n
CD68+ Mφ distribution
CD68+ cell count
Distance from Krt8hi transitional cells
o
Macrophages
CD68+ cells per field
Krt8lo/- field
Krt8hi field

Fig. 5

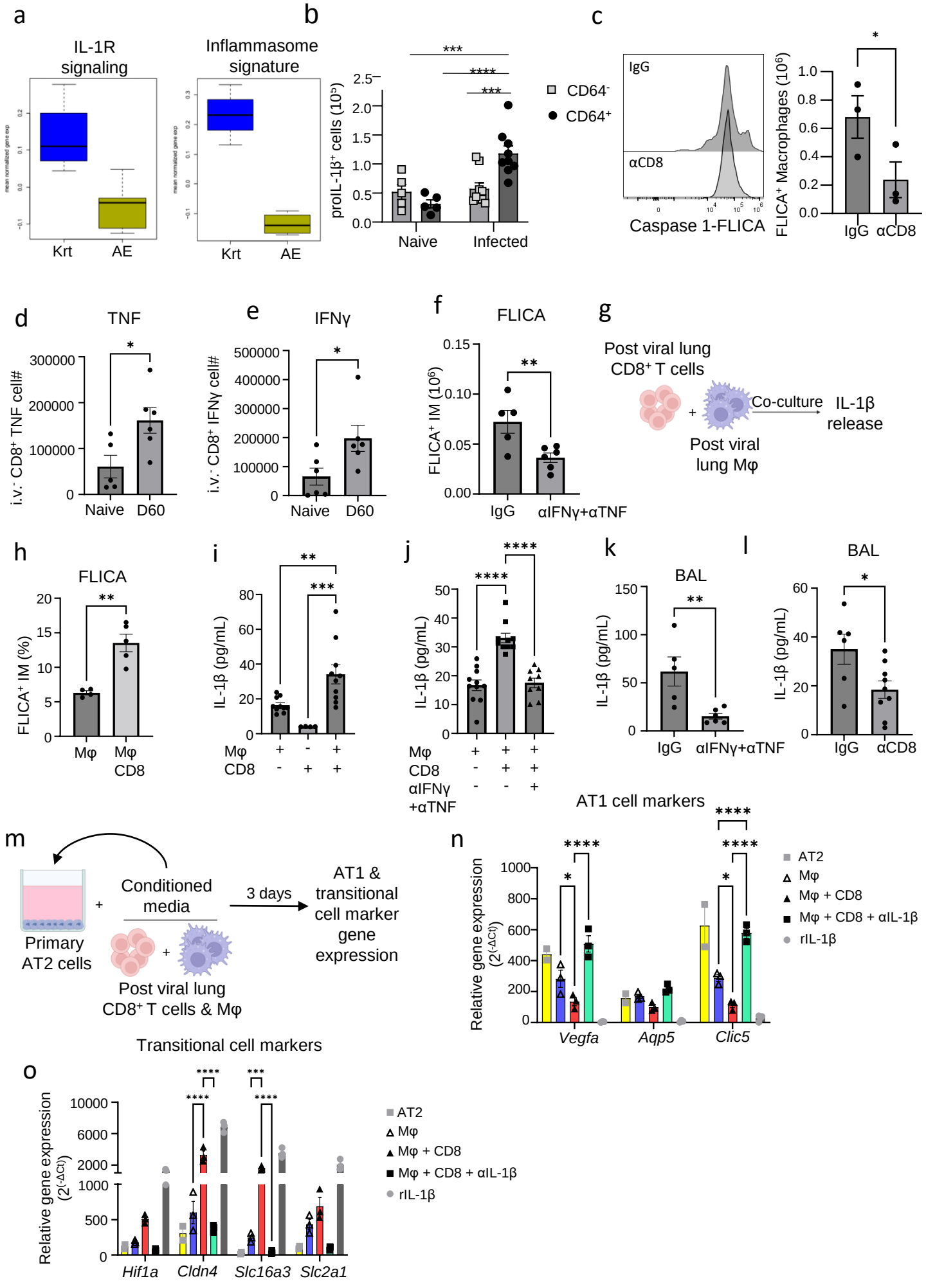
a
IL-1R signaling
Krt
AE
Inflammasome signature
Krt
AE
b
proIL-1β+ cells (10^5)
Naive
Infected
CD64-
CD64+
c
IgG
αCD8
Caspase 1-FLICA
FLICA+ Macrophages (10^6)
IgG
αCD8
d
TNF
i.v.- CD8+ TNF cell#
Naive
D60
e
IFNγ
i.v.- CD8+ IFNγ cell#
Naive
D60
f
FLICA
FLICA+ IM (10^6)
IgG
αIFNγ+αTNF
g
Post viral lung CD8+ T cells
Co-culture
IL-1β release
Post viral lung Mφ
h
FLICA
FLICA+ IM (%)
Mφ
Mφ CD8
i
IL-1β (pg/mL)
Mφ
CD8
j
IL-1β (pg/mL)
Mφ
CD8
αIFNγ +αTNF
k
BAL
IL-1β (pg/mL)
IgG
αIFNγ+αTNF
l
BAL
IL-1β (pg/mL)
IgG
αCD8
m
Primary AT2 cells
Conditioned media
Post viral lung CD8+ T cells & Mφ
3 days
AT1 & transitional cell marker gene expression
n
AT1 cell markers
Relative gene expression (2^(-ΔCt))
Vegfa
Aqp5
Clic5
AT2
Mφ
Mφ + CD8
Mφ + CD8 + αIL-1β
rIL-1β
o
Transitional cell markers
Relative gene expression (2^(-ΔCt))
Hif1a
Cldn4
Slc16a3
Slc2a1
AT2
Mφ
Mφ + CD8
Mφ + CD8 + αIL-1β
rIL-1β

# Fig. 6

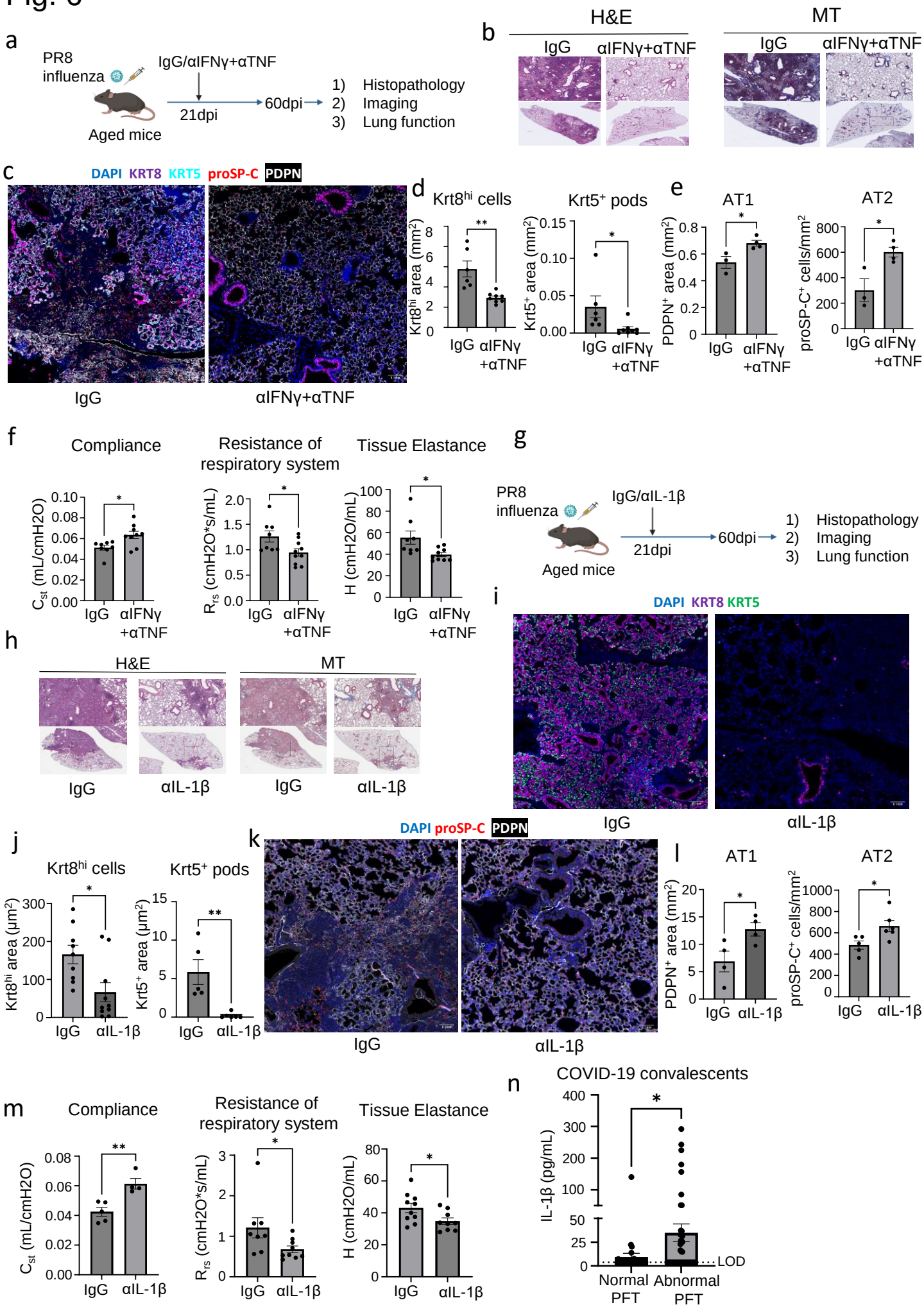
a
PR8 influenza
Aged mice
IgG/αIFNγ+αTNF
21dpi
60dpi
1) Histopathology
2) Imaging
3) Lung function
b
H&E
MT
IgG
αIFNγ+αTNF
c
DAPI KRT8 KRT5 proSP-C PDPN
IgG
αIFNγ+αTNF
d
Krt8hi cells
Krt5+ pods
Krt8hi area (mm2)
Krt5+ area (mm2)
IgG
αIFNγ +αTNF
e
AT1
AT2
PDPN+ area (mm2)
proSP-C+ cells/mm2
f
Compliance
Resistance of respiratory system
Tissue Elastance
Cst (mL/cmH2O)
Rrs (cmH2O*s/mL)
H (cmH2O/mL)
g
PR8 influenza
Aged mice
IgG/αIL-1β
21dpi
60dpi
1) Histopathology
2) Imaging
3) Lung function
h
H&E
MT
IgG
αIL-1β
i
DAPI KRT8 KRT5
IgG
αIL-1β
j
Krt8hi cells
Krt5+ pods
Krt8hi area (μm2)
Krt5+ area (μm2)
IgG
αIL-1β
k
DAPI proSP-C PDPN
IgG
αIL-1β
l
AT1
AT2
PDPN+ area (mm2)
proSP-C+ cells/mm2
m
Compliance
Resistance of respiratory system
Tissue Elastance
Cst (mL/cmH2O)
Rrs (cmH2O*s/mL)
H (cmH2O/mL)
n
COVID-19 convalescents
IL-1β (pg/mL)
LOD
Normal PFT
Abnormal PFT

# Extended data Fig.1

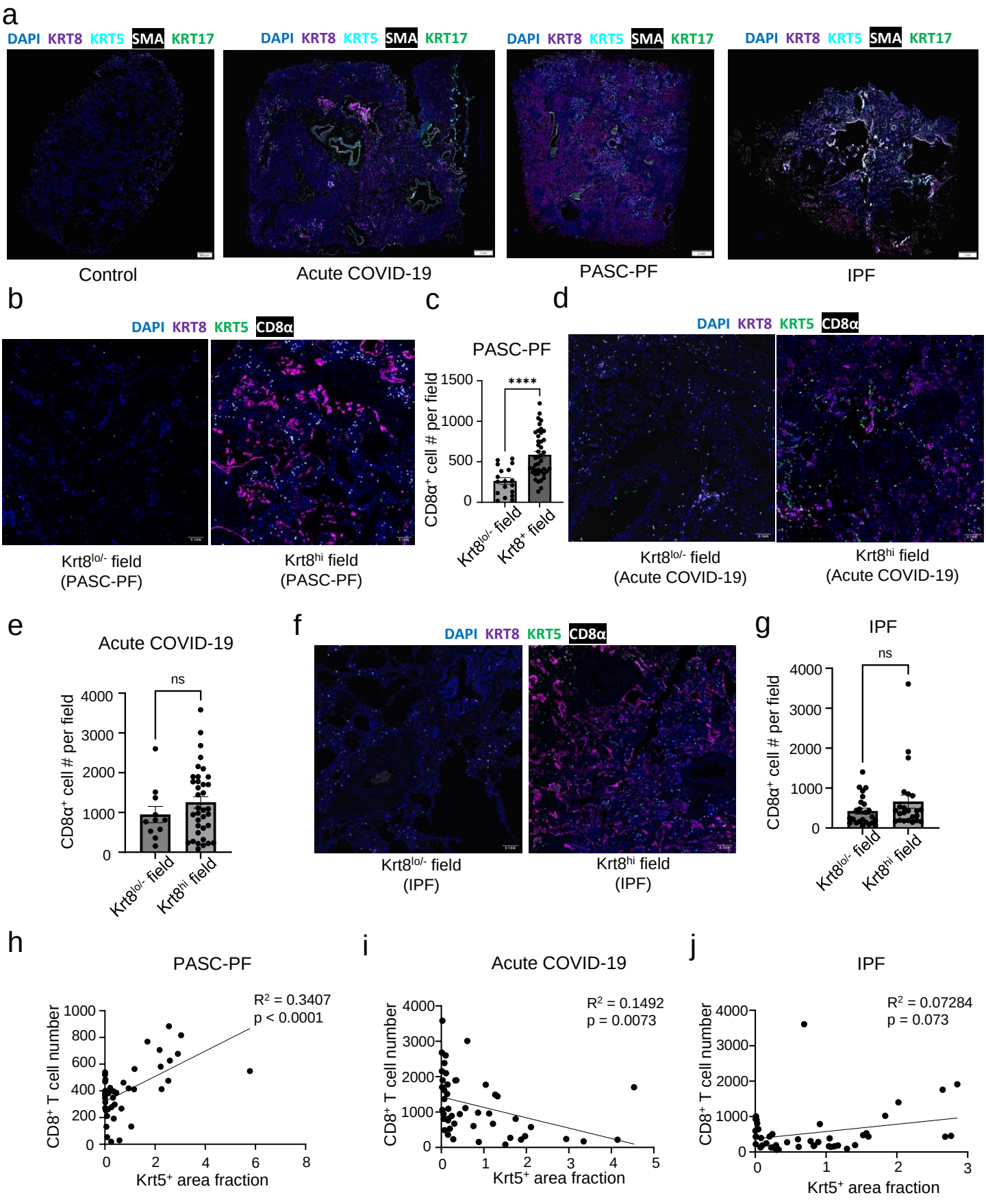

# Extended data Fig.2

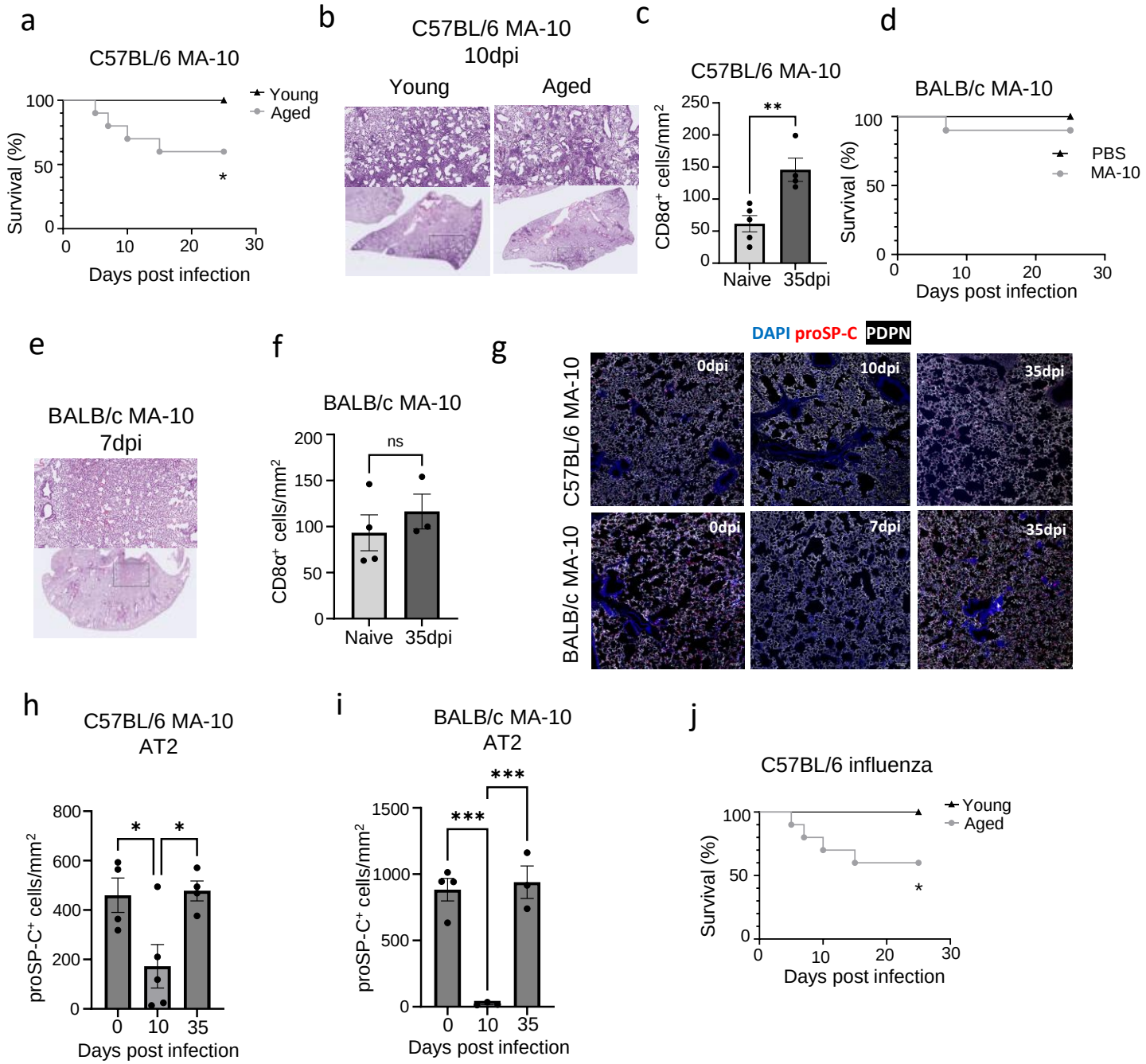

# Extended data Fig.3

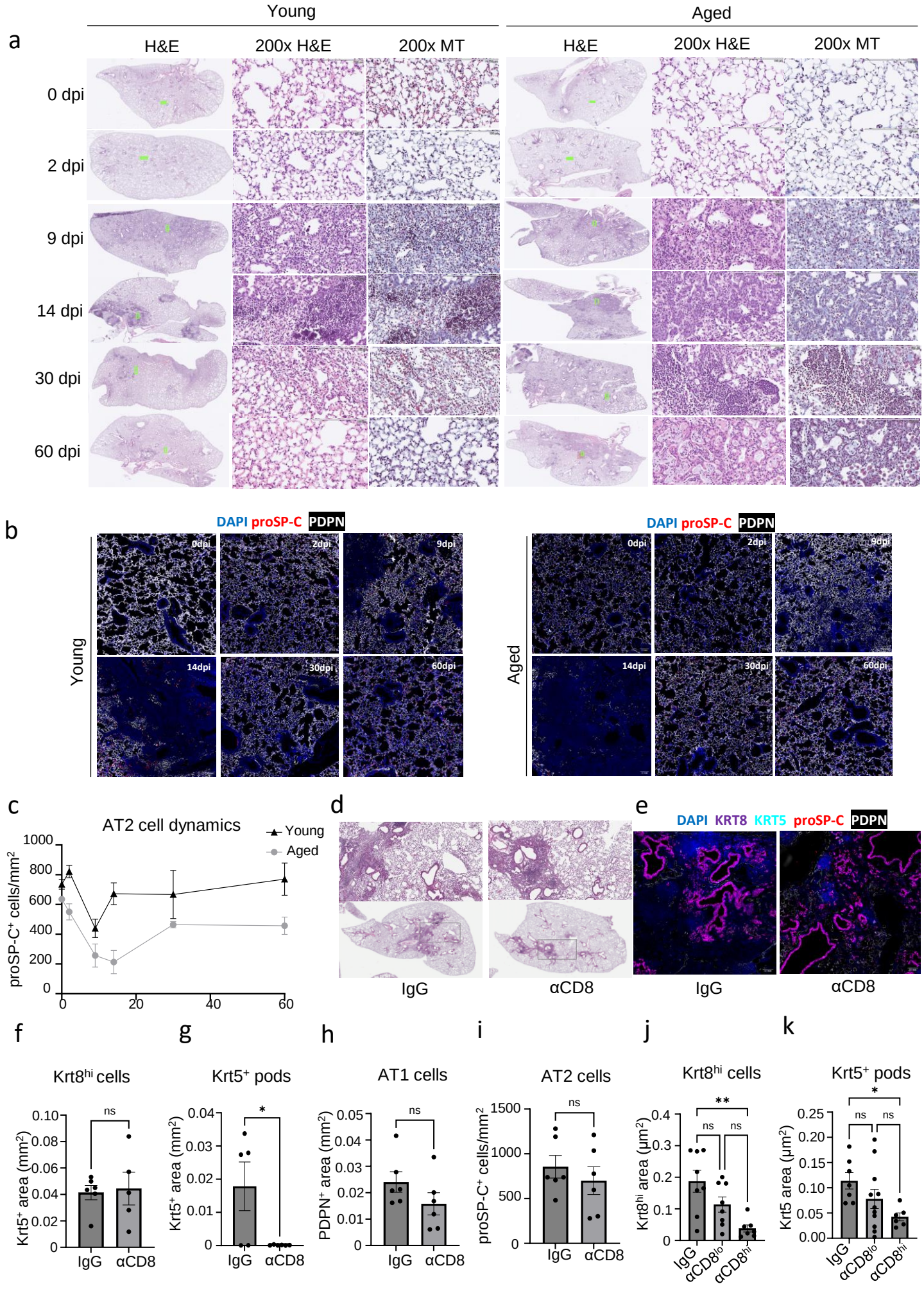

# Extended data Fig. 4

a

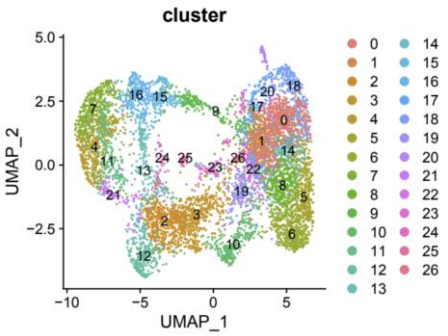


b

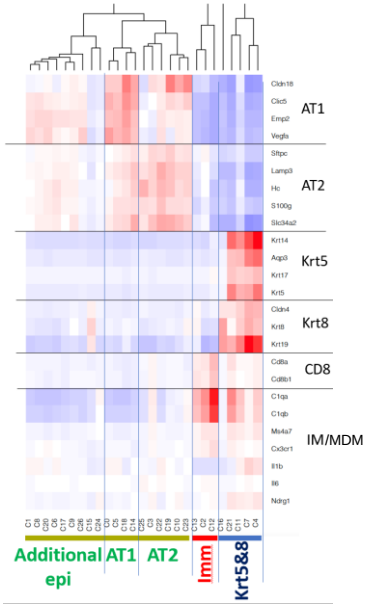


c

Fibrosis

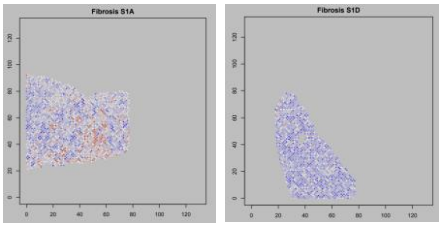


IgG αCD8

d Dysplastic epithelial progenitors

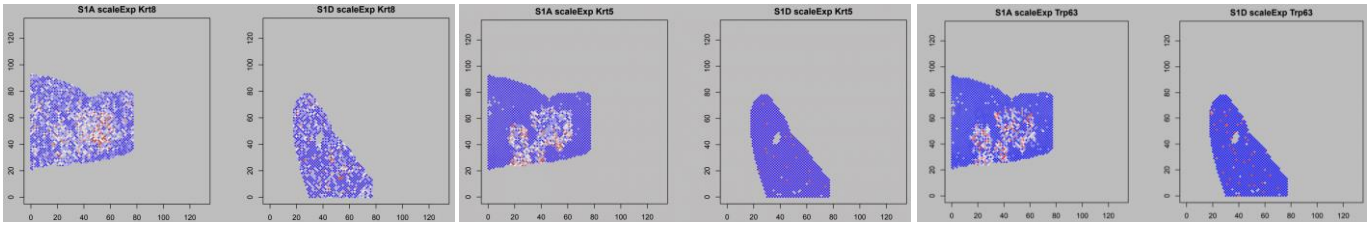


*Krt8* *Krt5* *Trp63*

e Alveolar epithelial cells

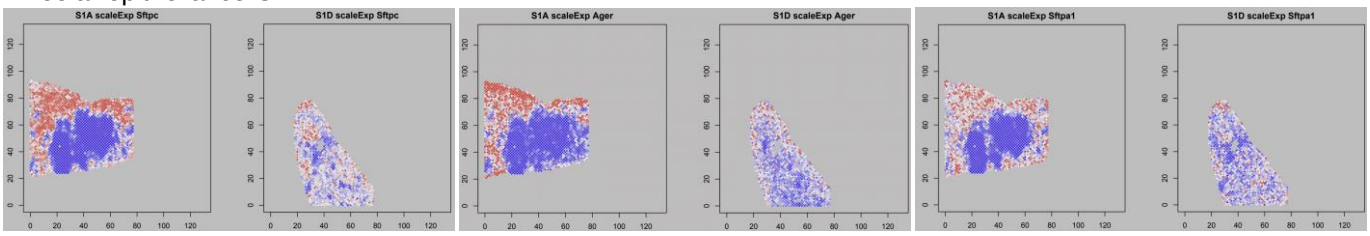


*Sftpc* *Ager* *Sftpa1*

f CD8⁺ T cells

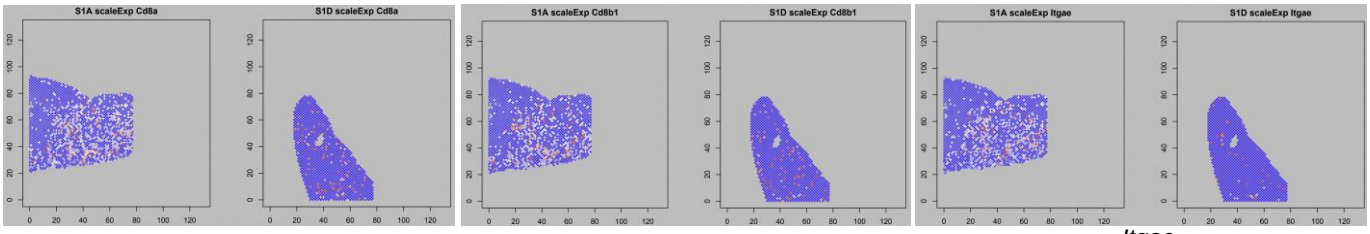


*CD8a* *CD8b1* *Itgae*

g Monocyte-derived macrophages

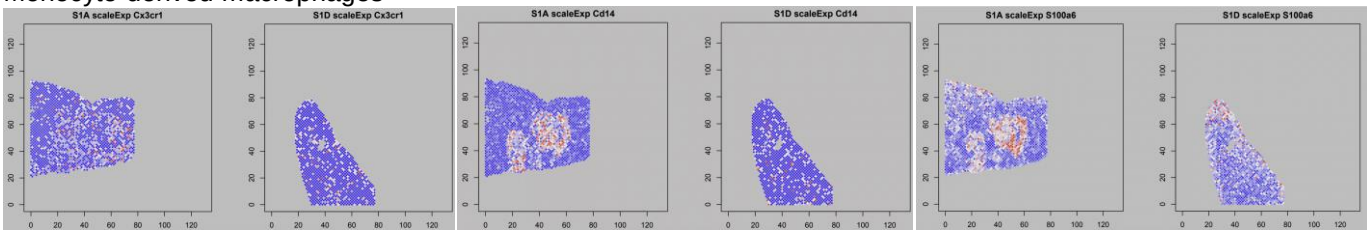


*Cx3cr1* *Cd14* *S100a6*

h Alveolar macrophages

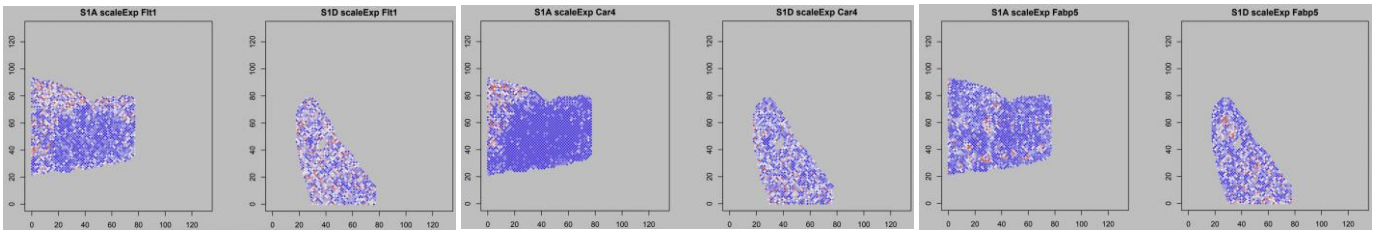


*Flt1* *Car4* *Fabp5*

# Extended data Fig. 5

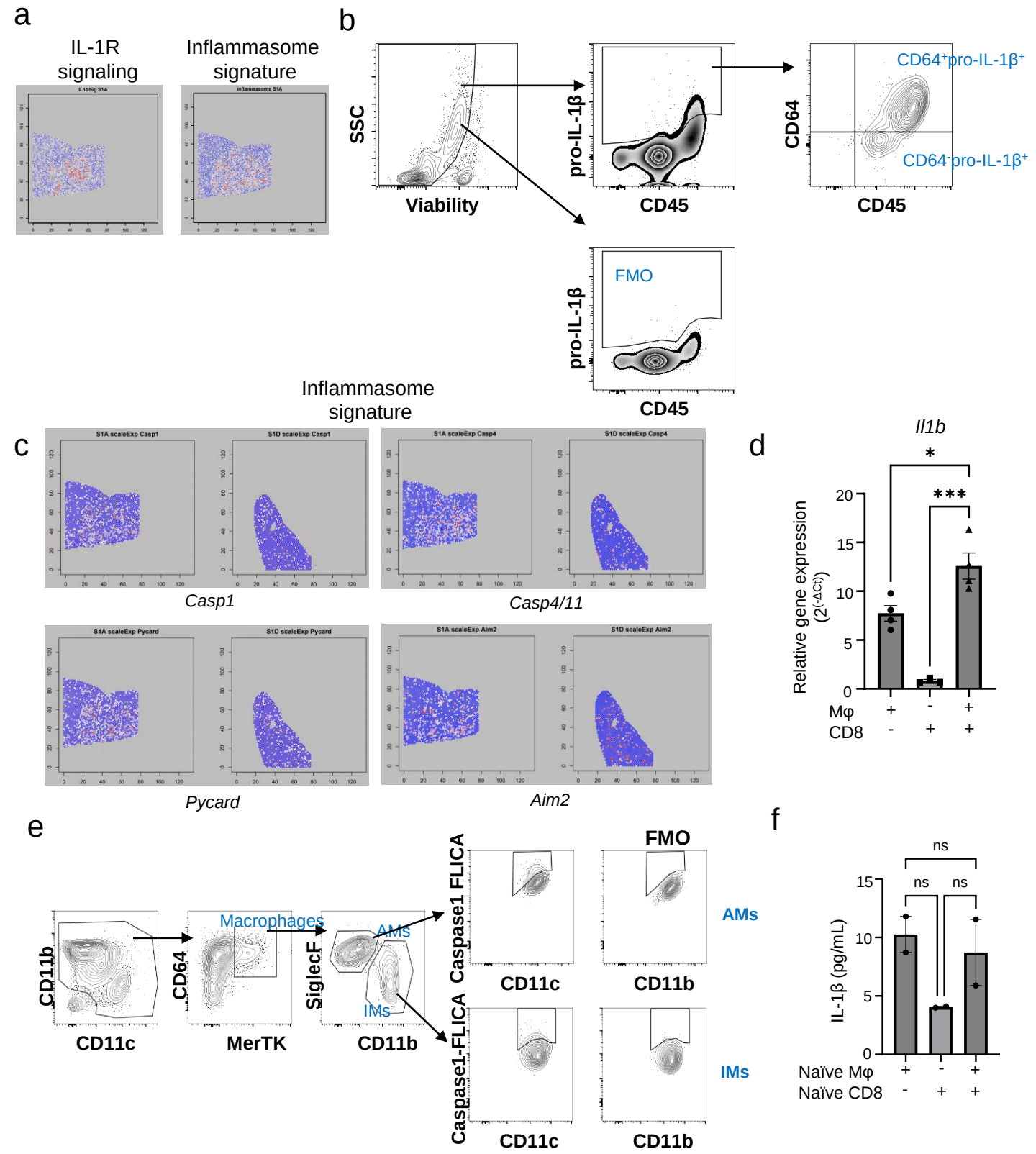

# Extended data Fig. 6

a

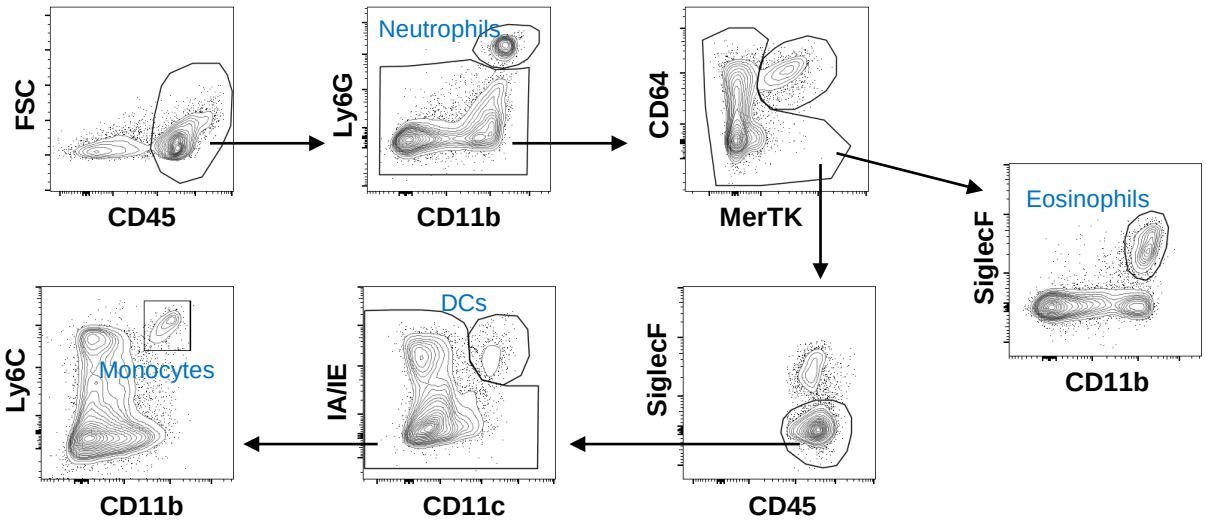


b

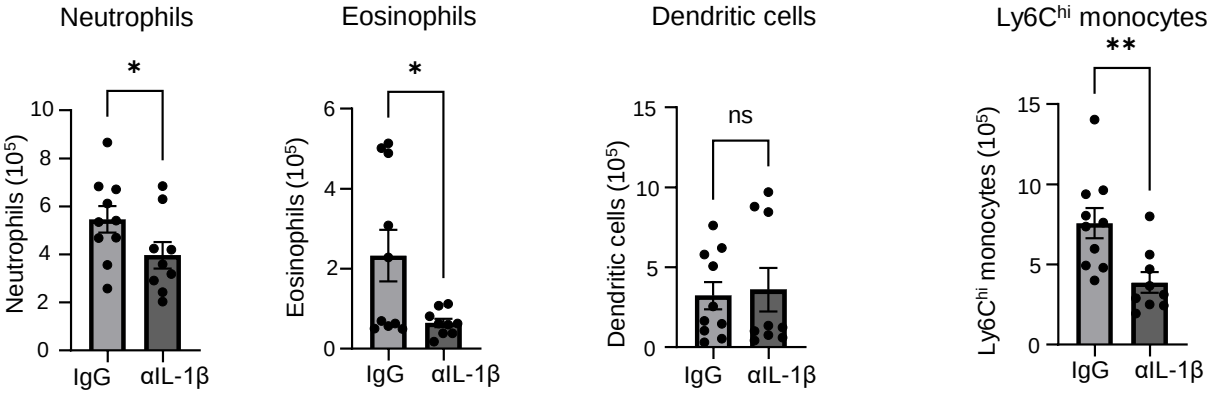


c

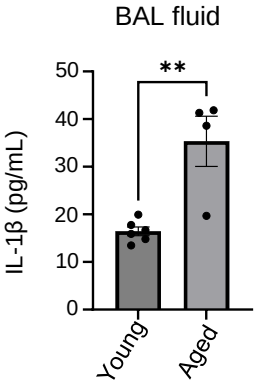


d

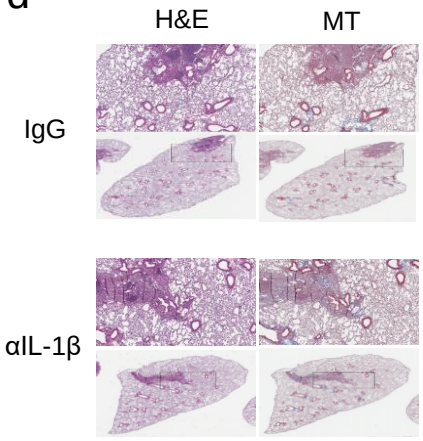

Extended data Fig. 7

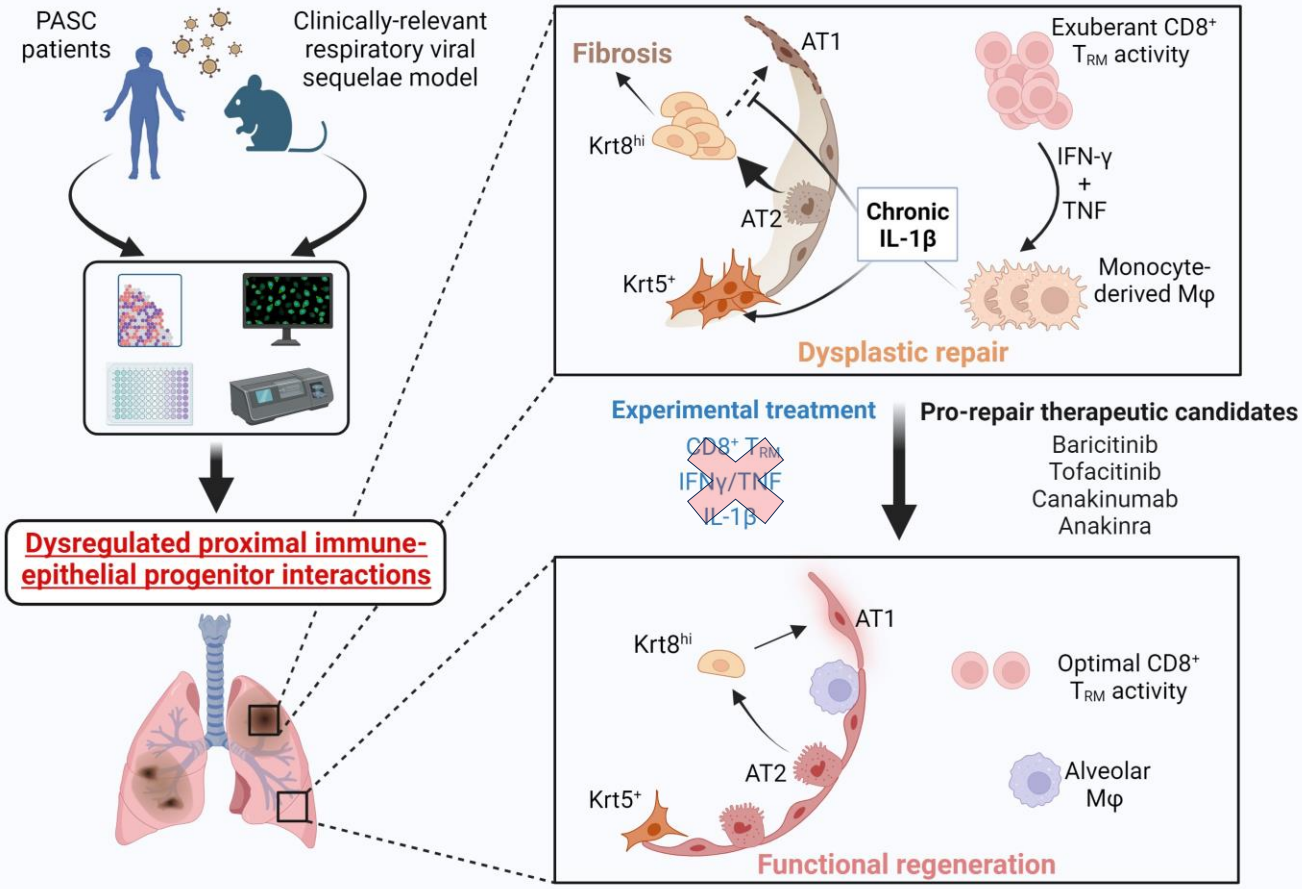

## Figure legends

**Fig.1 Spatial association between CD8$^+$ T cells and epithelial progenitors in human PASC-PF. a.** Representative H&E and Masson's Trichrome images of control and PASC-PF lung sections. **b.** Representative immunofluorescence images staining alveolar epithelial cell markers in control and PASC-PF lung sections. **c.** Quantification of AT1 (AGER$^+$) and AT2 (proSP-C$^+$) cells in control and PASC-PF lung sections (n = 5 control, 12 PASC-PF). **d.** Representative immunofluorescence images staining CD8$^+$ T cells (CD8α$^+$) and epithelial progenitors (Krt5$^+$ and Krt8$^{hi}$) in control and post-COVID pulmonary fibrosis lung sections. **e.** Quantification of Krt8$^{hi}$, Krt5$^+$, and **f.** CD8$^+$ T cells in control and PASC-PF lung sections (n = 15 control, 21 PASC-PF). **g.** Representative immunofluorescence images staining CD8$^+$ T cells and epithelial progenitors in acute COVID-19 and idiopathic pulmonary fibrosis (IPF) lung sections. **h.** Quantification of CD8$^+$ T cell number in control, acute COVID-19, PASC-PF, and IPF lung sections (n = 11 control, 6 Acute COVID-19, 19 PASC-PF, 13 IPF). **i.** Unbiased analysis of CD8$^+$ T cell distribution in a PASC-PF lung section. **j.** Simple linear regression of CD8$^+$ T cell number and Krt8$^{hi}$ area fraction in human PASC-PF, **k.** control, **l.** acute COVID-19, and **m.** IPF lung sections. Data are expressed as mean ± SEM. Statistical analyses were conducted using a two-tailed unpaired t-test (c,e,f) and an ordinary one-way ANOVA (h). *$p < 0.05$; **$p<0.01$; ***$p<0.001$; ****$p<0.0001$.

**Fig.2 Development of a mouse model of post-viral fibrosis recapitulating features of human PASC-PF. a.** Percent change in bodyweight of young (8-10 weeks) and aged (20-22 months) C57BL/6 mice post infection with $5x10^4$ PFU of SARS-CoV-2 MA-10 virus. **b.** Representative H&E and Masson's Trichrome images of young and aged C57BL/6 lungs post SARS-CoV-2 infection (35dpi) or PBS administration. **c.** Percent change in bodyweight of aged (12-14 months) BALB/c mice post infection with 1000PFU of SARS-CoV-2 virus or PBS treatment. **d.** Representative H&E and Masson's Trichrome images of aged BALB/c lungs post SARS-CoV-2 infection (35dpi) or PBS administration. **e.** Representative immunofluorescence images staining CD8$^+$ T cells (CD8α) and epithelial progenitors (Krt5$^+$ and Krt8$^{hi}$) in aged C57BL/6 and BALB/c mouse lungs post SARS-CoV-2 infection (35dpi). **f.** Quantification of Krt8$^{hi}$ area in aged C57BL/6 and BALB/c mice post SARS-CoV-2 infection (35dpi). **g.** Percent change in bodyweight of young (8-10 weeks) and aged (20-22 months) C57BL/6 mice post infection with 75PFU of PR8 influenza virus. **h.** Representative H&E and Masson's Trichrome images of young and aged C57BL/6 lungs post PR8 influenza virus infection (35dpi and 60dpi). **i.** Representative immunofluorescence images staining CD8$^+$ T cells (CD8α) and epithelial

progenitors (Krt5$^+$ and Krt8$^{hi}$) in young and aged C57BL/6 mouse lungs post H1N1 influenza A/PR8/34 virus infection (35dpi). **j.** Schematic of the FlexiVent system to evaluate pulmonary function in mice. **k.** Evaluation of compliance of the respiratory system in young and aged mice post PBS administration or influenza infection (60dpi).

**Fig.3 Persistent CD8$^+$ T cells impair functional alveolar regeneration and promote dysplastic lung repair. a.** Representative immunofluorescence images staining CD8$^+$ T cells (CD8α$^+$) and epithelial progenitors (Krt5$^+$ and Krt8$^{hi}$) in young and aged C57BL/6 mouse lungs over the course of influenza infection. **b.** Quantification of Krt8$^{hi}$, **c.** Krt5$^+$, and **d.** CD8$^+$ T cells in young and aged influenza-infected lung sections (n = 4 per time point). **e.** Unbiased analysis of CD8$^+$ T cell distribution in an aged mouse lung section post influenza infection (60dpi). **f.** Simple linear regression of CD8$^+$ T cell number and Krt8$^{hi}$ area fraction in influenza-infected mice at 9, 30, and 60dpi. **g.** Experimental design for CD8$^+$ T cell depletion post influenza infection. **h.** Representative H&E and Masson's Trichrome images of aged C57BL/6 lungs post influenza infection (60dpi) treated with αCD8 or control IgG antibody (Ab). **i.** Representative immunofluorescence images staining CD8$^+$ T cells (CD8α$^+$) and epithelial progenitors (Krt5$^+$ and Krt8$^{hi}$) in aged C57BL/6 mouse lungs post influenza infection (60dpi) treated with αCD8 or control IgG Ab. **j.** Quantification of Krt8$^{hi}$ and Krt5$^+$ area in aged influenza-infected lung sections treated with αCD8 or control IgG Ab. (n = 19 IgG control, 7 αCD8). **k.** Representative immunofluorescence images staining AT1 (PDPN$^+$) and AT2 (proSP-C$^+$) in aged C57BL/6 mouse lungs post influenza infection (60dpi), treated with αCD8 or control IgG Ab. **l.** Quantification of AT1 (PDPN$^+$) and AT2 (proSP-C$^+$) cells in aged influenza-infected lung sections treated with αCD8 or control IgG Ab. (n = 19 IgG control, 15 αCD8). **m.** Evaluation of static compliance ($C_{st}$) and **n.** resistance of the respiratory system ($R_{rs}$) in aged C57BL/6 mouse lungs post influenza infection (60dpi), treated with αCD8 or control IgG Ab.

**Fig4. Spatial transcriptomics reveal a CD8$^+$ T cell-macrophage-epithelial progenitor niche that drives dysplastic lung repair. a.** Representative H&E images of aged influenza-infected mice (60dpi) treated with control IgG Ab or αCD8 that were mounted on the 10X Visium slide. **b.** Visualization of CD8$^+$ T cells, Krt5$^+$ and Krt8$^{hi}$ transitional cells and alveolar epithelial cells based on gene signatures. **c.** Unbiased GSEA analysis of signaling pathways enriched in Krt5$^+$ and Krt8$^{hi}$-rich areas compared to healthy alveolar epithelium. **d.** Boxplots comparing gene expression signature of ADI/DATP/PATS and **e.** aberrant basaloid cells in Krt5$^+$ and Krt8$^{hi}$-rich areas and healthy alveolar epithelium. **f.** Gene expression signatures of various immune and epithelial cell types as well as signaling pathways in Krt5$^+$ and Krt8$^{hi}$-rich areas and healthy

alveolar epithelium. **g.** Heatmap of the physical distribution of $CD8^+$ T cells, monocyte-derived macrophages, alveolar macrophages, $Krt5^+$ and $Krt8^{hi}$ areas, and healthy alveolar epithelium. **h.** Unbiased analysis of the distribution of $CX3CR1^+$ macrophages in an aged influenza-infected (60dpi) lung section. **i.** Quantification of $CX3CR1^+$ cells within $Krt8^{-/lo}$ and $Krt8^{hi}$ fields in aged influenza-infected (60dpi) lungs (n=5). **j.** Representative immunofluorescence images of aged influenza-infected (60dpi) lungs treated with control IgG Ab or αCD8, staining monocyte-derived macrophages (CX3CR1) and epithelial progenitors (Krt5 and Krt8). **k.** Quantification of $CX3CR1^+$ macrophages in aged influenza-infected (60dpi) lungs (n=4). **l.** Representative immunofluorescence images of human PASC-PF lungs staining macrophages (CD68) and epithelial progenitors (Krt5 and Krt8). **m.** Quantification of $CD68^+$ macrophages in human control and PASC-PF lungs (n=11 control; 7 PASC-PF). **n.** Unbiased analysis of the distribution of $CD68^+$ macrophages in a human PASC-PF lung. **o.** Quantification of $CD68^+$ macrophages within $Krt8^{-/lo}$ and $Krt8^{hi}$ fields in human PASC-PF lungs (n=6).

**Fig.5 $CD8^+$ T cells promote macrophage-mediated IL-1β release via IFN-γ and TNF. a.** Boxplot of gene expression associated with IL-1R signaling and inflammasome components within healthy, and dysplastic ($Krt5^+$ and $Krt8^{hi}$) areas of aged influenza-infected mice (60dpi). **b.** Quantification of $proIL\text{-}1\beta^+$ cells in aged influenza-infected mice (42dpi) via flow cytometry. **c.** Assessment of caspase-1 activity in the lungs of aged influenza-infected mice (42dpi) after treatment with control IgG Ab or αCD8 by FLICA. **d.** Quantification of $TNF^+$ and **e.** $IFN\text{-}\gamma^+$ $CD8^+$ T cells in young and aged mice post influenza infection by flow cytometry. **f.** Assessment of caspase-1 activity in the lungs of aged influenza-infected mice (42dpi) after treatment with control Ab or αIFN-γ+αTNF by FLICA. **g.** Schematic of the *in vitro* macrophage and $CD8^+$ T cell coculture system. **h.** Assessment of caspase-1 activity following coculture by FLICA. **i.** Evaluation of IL-1β release into supernatant following coculture by ELISA. **j.** Evaluation of IL-1β release into supernatant following *in vitro* IFN-γ and TNF blockade in the coculture system. **k.** Evaluation of IL-1β levels in BAL fluid of aged PR8 influenza-infected mice (42dpi) after treatment with control IgG Ab or neutralizing αIFN-γ+αTNF. **l.** Evaluation of IL-1β levels in BAL fluid of aged influenza-infected mice (42dpi) after treatment with control IgG Ab or αCD8. **m.** Experimental design for 2D culture of primary murine AT2 cells for 3 days without/with conditioned media from macrophages, macrophages + $CD8^+$ T cells, macrophages + $CD8^+$ T cells + αIL-1β, and rIL-1β (positive control). **n.** Gene expression of AT1 cell markers 3 days post AT2 cell culture following exposure to conditioned media. **o.** Gene expression of transitional cell markers 3 days post AT2 cell culture following exposure to conditioned media.

**Fig.6 Therapeutic neutralization of IFN-γ and TNF, or IL-1β activity promotes alveolar regeneration and restores lung function. a.** Experimental design for *in vivo* IFN-γ + TNF neutralization post PR8 influenza infection. **b.** Representative H&E and Masson's Trichrome images of aged C57BL/6 lungs post PR8 influenza infection (42pi) treated with αIFN-γ + αTNF neutralizing Ab or control IgG Ab. **c.** Representative immunofluorescence images staining AT1 ($PDPN^+$), AT2 ($proSP\text{-}C^+$) and epithelial progenitors ($Krt5^+$ and $Krt8^{hi}$) in aged influenza-infected mice (42dpi) treated with αIFN-γ + αTNF neutralizing Ab or IgG control IgG Ab. **d.** Quantification of $Krt8^{hi}$ and $Krt5^+$ area and **e.** AT1 ($PDPN^+$) and AT2 ($proSP\text{-}C^+$) cells in aged influenza-infected mice treated with αIFN-γ + αTNF neutralizing Ab or IgG control IgG Ab (n= 3-6 IgG, 4-8 αIFN-γ + αTNF). **f.** Evaluation of static compliance ($C_{st}$), resistance of the respiratory system ($R_{rs}$), and tissue elastance (H) in aged influenza-infected mice treated with αIFN-γ + αTNF neutralizing Ab or control IgG Ab (n= 8 IgG, 10 αIFN-γ + αTNF). **g.** Experimental design for *in vivo* IL-1β blockade post influenza infection. **h.** Representative H&E and Masson's Trichrome images of aged C57BL/6 lungs post influenza infection (42pi) treated with αIL-1β or control IgG Ab. **i.** Representative immunofluorescence images staining epithelial progenitors ($Krt5^+$ and $Krt8^{hi}$) and **k.** AT1 ($PDPN^+$), AT2 ($proSP\text{-}C^+$) in aged C57BL/6 mouse lungs post influenza infection (42dpi) treated with αIL-1β or control IgG Ab. **j.** Quantification of $Krt8^{hi}$ and $Krt5^+$ areas, and **l.** AT1 ($PDPN^+$) and AT2 ($proSP\text{-}C^+$) cells in aged influenza-infected lung sections treated with αIL-1β or control IgG Ab (n= 9 IgG, 10 αIL-1β). **m.** Evaluation of static compliance ($C_{st}$), resistance of the respiratory system ($R_{rs}$), and tissue elastance (H) in aged influenza-infected lung sections treated with αIL-1β neutralizing antibody or control IgG antibody (n= 9 IgG, 10 αIL-1β). **n.** Evaluation of IL-1β levels in plasma of COVID-19 convalescents with or without abnormal lung function.

**Extended data Fig.1 Characterization of immune-epithelial progenitor interactions in human PASC-PF, acute COVID-19 and IPF lungs. (a)** Representative immunofluorescence images staining for myofibroblasts (αSMA) and aberrant epithelial progenitors (Krt5, Krt17, Krt8) in human control, acute COVID-19, PASC-PF and IPF lung sections. (**b)** Representative immunofluorescence images staining $CD8^+$ T cells in $Krt8^{-/lo}$ and $Krt8^{hi}$ areas within PASC-PF lungs. **(c)** Quantification of $CD8^+$ T cells in $Krt8^{-/lo}$ and $Krt8^{hi}$ areas within PASC-PF lungs. **(d)** Representative immunofluorescence images staining $CD8^+$ T cells in $Krt8^{-/lo}$ and $Krt8^{hi}$ areas within acute COVID-19 lungs. **(e)** Quantification of $CD8^+$ T cells in $Krt8^{-/lo}$ and $Krt8^{hi}$ areas within acute COVID-19 lungs. **(f)** Representative immunofluorescence images staining $CD8^+$ T cells in $Krt8^{-/lo}$ and $Krt8^{hi}$ areas within IPF lungs. **(g)** Quantification of $CD8^+$ T cells in $Krt8^{-/lo}$ and $Krt8^{hi}$ areas within IPF lungs. **(h)** Simple linear regression of $CD8^+$ T cell number and $Krt5^+$ area

fraction in PASC-PF, **(i)** acute COVID-19, and **(j)** IPF lung sections. Data are expressed as mean ± SEM. Statistical analyses were conducted using a two-tailed unpaired t-test. ****p<0.0001.

**Extended data Fig.2 Aged mice exhibit increased susceptibility to acute SARS-CoV-2 and influenza virus infection. (a)** Survival data of young and aged C57BL/6 following SARS-CoV-2 MA-10 infection. (**b)** Representative H&E images of young and aged C57BL/6 mice from the acute (10dpi) phase of SARS-CoV-2 MA-10 infection. (**c)** Quantification of $CD8^+$ T cell number from immunofluorescence images in naïve and SARS-CoV-2 MA-10 infected (35dpi) aged C57BL/6 mice. (**d)** Survival data of aged BALB/c following SARS-CoV-2 MA-10 infection. **(e)** Representative H&E images of aged BALB/c mice from the acute (10dpi) phase of SARS-CoV-2 MA-10 infection. (**f)** Quantification of $CD8^+$ T cell number from immunofluorescence images in naïve and SARS-CoV-2 MA-10 infected (35dpi) aged BALB/c mice. (**g)** Representative immunofluorescence images of aged C57BL/6 and BALB/c mouse lungs infected with SARS-CoV-2 MA-10, staining alveolar epithelial cell markers (AT1- PDPN; AT2 – proSP-C). **(h)** Quantification of proSP-$C^+$ AT2 cells in aged C57BL/6 and **(i)** BALB/c mouse lungs post SARS-CoV-2 MA-10 infection. **(j)** Survival data of young and aged C57BL/6 following PR8 influenza virus infection.

**Extended data Fig.3 Chronic pathology and tissue sequelae after influenza infection. (a)** Representative H&E and MT images of young and aged C57BL/6 influenza-infected mouse lungs over the course of infection. **(b)** Representative immunofluorescence images of young and aged C57BL/6 influenza-infected mouse lungs, staining alveolar epithelial cell markers (AT1- PDPN; AT2 – proSP-C) over the course of influenza infection. **(c)** Quantification of AT2 (proSP-$C^+$) cell numbers in young and aged mice over the course of influenza infection (n= 4 per timepoint) **(d)** Representative H&E images of young C57BL/6 lungs post influenza infection (60dpi) treated with αCD8 or control IgG Ab. **(e)** Representative immunofluorescence images of young C57BL/6 lungs post influenza infection (60dpi) treated with αCD8 or control IgG Ab. **(f)** Quantification of $Krt8^{hi}$, **(g)** $Krt5^+$, **(h)** AT1 cells, and **(i)** AT2 cells in young influenza-infected mouse lungs, treated with αCD8 Ab or control IgG Ab. **(j)** Quantification of $Krt8^{hi}$ and **(k)** $Krt5^+$ area in aged influenza-infected mouse lungs, treated with control Ab, low dose αCD8 Ab or high dose αCD8 Ab.

**Extended data Fig.4 Spatial gene expression with or without $CD8^+$ T cell depletion. (a)** UMAP visualization of spatial transcriptomics data from aged influenza-infected mice (60dpi), treated with control IgG Ab (N=2) or αCD8 (N=2). **(b)** Heatmap of gene expression across all

identified clusters of spots. **(c)** Spatial map of the expression of genes associated with lung fibrosis in aged influenza-infected mice (60dpi), treated with control IgG Ab (S1A) or αCD8 (S1D). **(d)** Spatial map of the expression of dysplastic epithelial progenitors (*Krt8, Krt5, Trp63*), **(e)** alveolar epithelial (*Sftpc1, Ager, Sftpa1*), **(f)** $CD8^+$ T cell (*CD8a, CD8b1, Itgae*), **(g)** monocyte-derived macrophages (*Cx3cr1, Cd14, S100a6*), and **(h)** alveolar macrophage (*Flt1, Car4, Fabp5*) marker genes in aged influenza-infected mice (60dpi), treated with control Ab (S1A) or αCD8 (S1D).

**Extended data Fig.5 Inflammasome-mediated IL-1β release by macrophages in areas of dysplastic repair. (a)** Spatial map of IL-1R signaling and inflammasome signature in healthy, and dysplastic ($Krt5^+$ and $Krt8^{hi}$) areas of aged influenza-infected mice (60dpi. **(b)** Gating strategy to identify proIL-$1\beta^+$ cells following infection of aged C57BL/6 mice. **(c)** Spatial map of inflammasome-associated genes (*Casp1, Casp4/11, Pycard*, and *Aim2*) in aged influenza-infected mice (60dpi) treated with control Ab (S1A) or αCD8 (S1D). **(d)** Quantification of IL-1β gene expression in following macrophage and $CD8^+$ T cell coculture. **(e)** Gating strategy to identify $FLICA^+$ cells following infection of aged C57BL/6 mice. **(f)** Evaluation of IL-1β release into the supernatant following isolation and coculture of macrophages and $CD8^+$ T cells from naïve aged C57BL/6 mice.

**Extended data Fig.6 Lung inflammatory immune populations following IL-1β blockade. (a)** Gating strategy to identify various innate immune cell populations in aged influenza-infected C57BL/6 mice. **(b).** Quantification of neutrophils, eosinophils, dendritic cells and monocytes in aged influenza-infected (42dpi) mice following treatment with control Ab or αIL-1β neutralizing Ab. **(c)** Evaluation of IL-1β levels in BAL fluid in young and aged mice post influenza infection (42dpi). **(d)** Representative H&E and Masson's Trichrome images of young C57BL/6 lungs post influenza infection (42pi) treated with αIL-1β or control IgG Ab.

**Extended data Fig.7 Dysregulated immune-epithelial progenitor interactions drive post-viral sequelae in PASC.**

**Supplementary Table1. Clinical information of the PASC-PF cohort.**

| Patient # | Duration of hospitalization during acute COVID-19 (Days) | Number of COVID-19 infections | Home $O_2$ supplement | Days from COVID-19 infection to lung transplant (Days) | CT Chest findings (pre-transplant) |
|---|---|---|---|---|---|
| 1 | 30 | 4 | Yes | 109 | 1. Moderate left loculated hemothorax and bilateral pneumothoraxes.<br>2. Residual extensive bilateral COVID pneumonia/ARDS. |
| 2 | 4 | 1 | Yes | 566 | 1. Persistent bronchiectasis, volume, and architectural distortion in upper lobes.<br>2. Stable bi-apical cystic structures with communicating bronchi.<br>3. Loculated left pneumothorax and bilateral pleural effusion |
| 3 | 20 | 1 | No | 434 | 1. Diffuse areas of central bronchiectasis extending to the peripheries of both lungs with diffuse ground glass opacification.<br>2. Upper lobe predominant curvilinear areas of opacification suggesting fibrosis and scarring.<br>3. A 5 mm right upper lobe calcified granuloma. |
| 4 | 90 | 1 | Yes | 456 | 1. Cystic bronchiectasis in the right upper lobe on a background of diffuse ground glass opacification, which may be sequela of COVID-19, though not typical.<br>2. Probable recurrent infection in the right upper lobe accounts for this appearance. Distribution is inconsistent with UIP. |
| 5 | 149 | 1 | Hospitalized until lung transplant | 149 | 1. Moderate-sized bilateral apical pneumothoraxes.<br>2. Diffuse ground-glass opacification and bronchial retraction with subpleural blebs in this patient with known COVID-19 pneumonia and clinically confirmed ARDS, likely organizing/exudative phase and with possible diffuse alveolar damage.<br>3. Trace bilateral pleural effusions.<br>4. Mildly enlarged multi compartmental mediastinal lymph nodes are likely reactive. |
| 6 | Unknown | 1 | Yes | 230 | 1. Small bleb in the left upper lobe.<br>2. Extensive interstitial ground-glass opacities as well as curvilinear consolidation likely related to sequelae from known Covid pneumonia. |
| 7 | Unknown | 1 | Yes | 148 | 1. There is evidence for pulmonary fibrosis with traction bronchiectasis and honeycombing |

| | | | | | |
|---|---|---|---|---|---|
| | | | | | there is involvement of upper mid and lower lung zones.<br>2. Some increasing opacity and ground-glass of the bases may be progressive disease versus some superimposed active alveolitis.<br>3. There is mild mediastinal and hilar lymphadenopathy. |
| 8 | 90 | 2 | Yes | 902 | 1. Chronic interstitial lung diseases.<br>2. Bilateral bronchiectasis greater on the right.<br>3. Reticular ground glass opacities in both lungs. |
| 9 | 6 | 1 | Yes | 817 | 1. Diffuse bilateral pulmonary interstitial thickening, and bronchiectasis, most pronounced at the right lower lobe. |
| 10 | Unknown | 2 | Yes | 150 | 1. Bilateral moderate to severe bronchiectasis centrally with areas of diffuse and severe peribronchial wall thickening especially in the lower lobes with several areas of mucous plugging.<br>2. Minimal areas of ground glass patchy airspace opacities are present within the left upper lobe and superior segment of the right lower lobe. |
| 11 | Unknown | 1 | Yes | 300 | 1. Peripheral and peri-bronchovascular reticulations and textured ground-glass opacities without honeycombing, with associated architectural and pleural-parenchymal interface distortion, traction bronchiectasis and bronchiectasis, and regional volume loss, compatible with pulmonary fibrosis. |
| 12 | Unknown | 1 | Yes | 53 | 1. A couple of < 5 mm right middle lobe calcified granulomas.<br>2. Extensive ILD likely sequelae of C19 pneumonia with diffuse ground-glass throughout the lungs. |
| 13 | 38 | 2 | Intubated | 92 | 1. Dense consolidation with wedge-shaped areas of scarring are present bilaterally. Dense air bronchograms are present.<br>2. There is an air-containing cysts seen within the right middle lobe.<br>3. There is a specific mucus seen within the trachea and right mainstem bronchus. |
| 14 | 60 | 1 | Yes | 80 | 1. Consolidations within the upper anterior segments bilaterally, w/ associated cystic traction bronchiectasis.<br>2. Diffuse consolidative and ground glass opacities throughout the remainder of the lungs. |

| | | | | | |
|---|---|---|---|---|---|
| | | | | | 3. Large left pneumothorax with multiple adhesions along the anterior left upper lobe.<br>4. Small left pleural effusion.<br>5. Small right hydropneumothorax. |
| 15 | 201 | 1 | Hospitalized until lung transplant | 201 | 1. Severe dense consolidation of both lungs with air bronchograms.<br>2. The right lung is collapsed with a right hydropneumothorax present.<br>3. Small left pleural effusion |
| 16 | 58 | 2 | Yes | 120 | 1. Severe diffuse parenchymal lung consolidation with severe volume loss.<br>2. Moderate size loculated left pleural effusion and small loculated right pleural effusion. |
| 17 | 20 | 1 | Yes | 329 | 1. Evidence of interstitial fibrosis manifested by predominantly subpleural upper zone reticulations and traction bronchiectasis with scattered areas of geographic perfusion and ground-glass opacities. This is all most likely residual of the patient's known Covid pneumonia. |
| 18 | 0 | 1 | Yes | 748 | 1. Extensive changes of pulmonary fibrosis in the right greater than left lungs characterized by bibasilar predominant bronchiectasis, reticulation and honeycombing in near total involvement of the right lung with some relative sparing at the right lung apex. Extensive involvement of the left lower lobe and lingula with the left upper lobe slightly less involved. |

**Supplementary Table2. Antibodies and reagents.**

| **Antibody Target** | **Source** | **Identifier** |
|---|---|---|
| Rat anti-cytokeratin 8 (TROMA-1) | DSHB | Antibody Registry ID: AB 531826 |
| Rabbit anti-proSP-C | Millipore Sigma | Cat#: AB3786 |
| Hamster anti-PDPN | Abcam | Cat#: ab11936 |
| Chicken anti-cytokeratin 5 (human) | BioLegend | Cat#: 905901 |
| Chicken anti-cytokeratin 5 (mouse) | BioLegend | Cat#: 905903 |
| Rabbit anti-CD8α (human) | Cell Signaling Technologies | Cat#: 85336S |
| Rabbit anti-CD8α (mouse) | Cell Signaling Technologies | Cat#: 98941S |
| Rabbit anti-cytokeratin 17 | Millipore Sigma | Cat#: HPA000453 |

| | | |
|---|---|---|
| Mouse anti-SMA | Millipore Sigma | Cat#: A5528 |
| Rabbit anti-AGER | Proteintech | Cat#: 16346-1-AP |
| Mouse anti-CD68 | Abcam | Cat#: Ab955 |
| Mouse anti-proSP-C | Santa Cruz | Cat#: sc-518029 |
| Rabbit anti-CX3CR1 | ThermoFisher | Cat#: 14-6093-81 |
| DyLight 649 Donkey anti-rabbit IgG | BioLegend | Cat#: 406406 |
| Donkey anti-chicken IgGY (H+L) Alexa Fluor 488 IgG (H+L) | ThermoFisher | Cat#: A78948 |
| Goat anti-rat IgG (H+L) Alexa Fluor 555 | ThermoFisher | Cat#: A48270 |
| Goat anti-Armenian Hamster IgG (H+L) Alexa Fluor 488 | ThermoFisher | Cat#: A78963 |
| Goat anti-Chicken IgY (H&L) Alexa Fluor 750 | Abcam | Cat#: ab175755 |
| Goat anti-rat IgG (H+L) Alexa Fluor 488 | ThermoFisher | Cat#: A-11006 |
| Goat anti-rabbit IgG (H+L) Alexa Fluor 488 | ThermoFisher | Cat#: A-11008 |
| Viability dye (Zombie NIR) | BioLegend | Cat#: 423105 |
| Viability dye (Zombie Aqua) | BioLegend | Cat#: 423101 |
| CD8a-BV510 (53-6.7) | BioLegend | Cat#: 100751 |
| CD11b-BV510 (M1/70) | BioLegend | Cat#: 101245 |
| CD11b-PerCP/Cy5.5 (M1/70) | BioLegend | Cat#: 101227 |
| CD11c-BV421 (N418) | BioLegend | Cat#: 117329 |
| CD45-BV605 (30-F11) | BioLegend | Cat#: 103139 |
| CD64-BV711 (X54-5/7.1) | BioLegend | Cat#: 139311 |
| IA/IE–PerCP/Cy5.5 (M5/114.15.2) | BD Biosciences | Cat#: 556999 |
| IL-1b-PE (NJTEN3) | eBioscience | Cat#: 12-7114-82 |
| Ly6C-PE (HK1.4) | BioLegend | Cat#: 128007 |
| Ly6G-PE/Cy7 (1A8) | BioLegend | Cat#: 127617 |
| MerTK-APC (2B10C42) | BioLegend | Cat#: 151507 |
| Influenza $NP_{366-374}$-APC | NIH | IEDB ID: 4602 |
| SiglecF-APC/Cy7 (E50-2440) | BD Biosceinces | Cat#: 155531 |
| CD45-APC (30-F11) | BioLegend | Cat#: 103111 |
| EpCAM/CD326 – PerCP/Cy5.5 (G8.8) | BioLegend | Cata#: 118219 |
| IA/IE-FITC (M5/114.15.2) | BioLegend | Cat# : 107605 |